NTNU

Norwegian University of
Science and Technology

Inductor Design for Filter Applications with high dV/dt

Yngve Berset Solbakken

Master of Science in Electric Power Engineering
Submission date: July 2016
Supervisor: Roy Nilsen, ELKRAFT

Norwegian University of Science and Technology
Department of Electric Power Engineering

Problem description

Recent development in power electronic components has given rise to switching devices based on silicon and carbide (SiC) which can increase efficiency.

It makes switching possible at much higher frequencies and with very short rise time. Due to this, output filters are needed to protect cables and connected equipment from reflections and voltage doubling.

The project work preceding this thesis designed a passive electrical filter in that regard. Based on that filter, this work will focus on design of the filter inductor itself.

Due to the fast rise time from SiC converters, it is important to design components with decreased stray capacitances to avoid compromising the filter performance and draw unnecessary current from the switching devices.

The work will be concentrated on designing a compact and cost effective filter inductor both for DC/DC converters and active frond-end converters by discussion and analysis of the following aspects:

- Specify typical inductor value, current and voltage rating.
- Study type of preferable inductor designs with regards to minimal stray capacitances.
- Choice of magnetic material and type of windings.
- Numerical analysis in finite element software.

Abstract

The work in this report has consisted in the design of three different inductors to verify how conductor profile impact stray capacitance, and how stray capacitance impact filtering performance.

The three conductor profiles were flat helical, vertical helical and circular.

By use of 3D-design and numerical computations in COMSOL Multiphysics, three inductors with the different conductor profiles has been created. Simplified 2D and 3D-models based on these were used to extract flux density and stray capacitance in numerous parametric sweeps.

The inductor parameters were later employed in a SIMULINK model to evaluate how the inductors, with their stray capacitance, performed in a dV/dt-filter.

Of the three conductor profiles, the flat helical profile exhibited the highest stray capacitance. The lowest stray capacitance was found in the circular conductor profile.

It was found that when the stray capacitance exceeds approximately 200 pF, reflections and voltage doubling occur at the filter output.

At minimum distance between turns, the flat helical profile had a stray capacitance of 543 pF. The vertical helical profile, had 217 pF and the circular profile, 71 pF.

Measures to decrease stray capacitance is discussed and simulated, and modified inductors are re-tested in SIMULINK to verify that reflections are mitigated.

Abstract (Norwegian)

Arbeidet i denne rapporten har bestått av å utforme ulike filterspoler for å undersøke hvordan viklingens lederprofil innvirker på parasittiske kapasitanser, og hvordan dette påvirker filterets ytelse.

Tre forskjellige lederprofiler er modellert og testet; flat spiralformet, stående spiralformet og sirkulær spiralformet leder.

Ved bruk av tredimensjonal design og numeriske beregninger i COMSOL Multiphysics er det konstruert tre spoler med de ulike viklingsprofilene. Forenklede 2D og 3D-modeller basert på disse ble benyttet til å beregne flukstetthet og strøkapasitans i tallrike parametersveip.

Induktansparameterne, sammen med strøkapasitansene, ble videre benyttet i en SIMULINK-modell for at vurdere spolenes yteevne i et dV/dt-filter.

Av de tre lederprofilene ble det funnet ut at flat spiralformet leder har høyest strøkapasitans med 543 pF. Stående spiralformet hadde 217 pF og den sirkulære profilen 71 pF.

Det ble konstatert at når strøkapasitansen overstiger ca. 200 pF, vil det forekomme refleksjoner og spenningsfordobling ved filterutgangen og på tilkoblet utstyr.

Foranstaltninger for å redusere strøkapasitans er diskutert og simulert, og modifiserte spoler er re-testet i SIMULINK for å verifisere at refleksjonene opphørte.

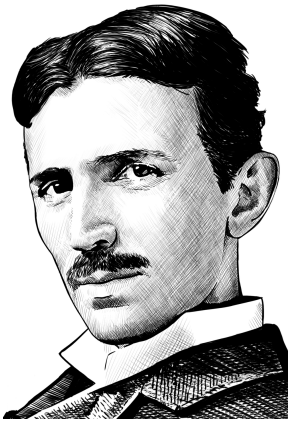

Is there, I ask, can there be, a more interesting study than that of alternating currents ? In all these investigations, in all these experiments, which are so very, very interesting for many years past — ever since the greatest experimenter who lectured in this hall discovered its principle — we have had a steady companion, an appliance familiar to every one, a plaything once, a thing of momentous importance now — the induction coil.

— Nikola Tesla (Excerpt from a speech delivered before the Institution of Electrical Engineers in London, February 1892)

Preface

This report is the result of my master's thesis work at Norwegian University of Science and Technology (NTNU) and is written in co-operation with Wärtsilä Norway AS during the spring semester of 2016.

It is a continuation of my project report about filter design for fast switching devices written last semester. The focus is now directed at the design of the filter inductor in conjunction with fast rise time and stray capacitance.

The work has been conducted in the finite element computation software COMSOL and later tested in MATLAB.

It has been a semester filled with both frustration and blissfulness alternating each other while learning the hard way how magnetic fields and numerical software works.

My time at NTNU has been the best time of my life till now, and I will miss the incredible fast and steady flow of knowledge I have experienced.

I will also miss all my great buddies whom I have shared exam problems and exam beers with. You guys made a huge difference!

Yngve Solbakken
July 11, 2016

Acknowledgments

Firstly, I wish to thank my supervisor, professor Roy Nilsen. I sincerely appreciate all the times you have left your office door open for me to come in with all my questions, and let me walk out again with all the missing pieces (and some extra). Thank you for giving me such large amounts of freedom in my work with this thesis.

In addition, the following people have assisted me in my work presented in this report:

- Professor Robert Nilssen by teaching me about magnetic and electric fields in the most fabulous of ways - both in the auditoriums and in the afternoons when single questions at your office became a journey into Einstein's world of relativity lasting long past working hours.
- Frode Jenset at Wärtsilä Norway by providing valuable insight into industrial and practical inductor design considerations.
- My fellow student, Eirik Haustveit, by always serving great answers and setting of time to discuss my thoughts. And for being a fantastic combination of a person and an abacus; a friend one can count on.
- Arve Dispen at the Heterogeneous & Parallel Computing group (HPC/NOTUR) by assisting me in running COMSOL simulations on Norway's largest supercomputer; Vilje.

I express my thankfulness for the use of *Vilje* and NTNU's computational resources provided by NOTUR.

This page is for Mai-Linn,

the girl who started off as my student assistant in power electronics and later aspired to become my personal teacher, my mentor and ultimately my girlfriend and best buddy.

Without her, I would not have been able to pull this through.

Without her, you would not be reading this.

I am forever thankful.

Contents

Acronyms

Acronyms used in this report together with the page where they are first used.

SiC Silicon Carbide 5

EMI Electromagnetic Interference 32

PWM Pulse-Width Modulation 5

FEM Finite Element Method xvi

MPP MolyPermalloy Powder 37

SEM Scanning Electron Microscope

Nomenclature

$\boldsymbol{B}$	Magnetic flux density
$\boldsymbol{H}$	Magnetic flux strength / field intensity
$\boldsymbol{J}$	Current density
$\boldsymbol{M}$	Magnetization
χ_m	Magnetic susceptibility
ϵ_0	Permittivity of vacuum, defined as $\frac{1}{\mu_0 c_0} \approx 8.8542 \times 10^{-12}\,\mathrm{F \cdot m^{-1}}$
$\hat{V}_{max}$	Maximum voltage recorded at motor terminal
$\mathfrak{F}$	Magnetomotive force
$\mathfrak{R}$	Magnetic reluctance
μ	Combined permeability
μ_0	Permeability of vacuum: $4\pi \times 10^{-7}\,\mathrm{H \cdot m^{-1}}$
μ_r	Relative permeability
ω_c	Cutoff frequency
ϕ	Magnetic flux
ζ	Relative damping ratio
c_0	Defined value for speed of light: $299\,792\,458\,\mathrm{m \cdot s^{-1}}$
C_f	Filter capacitor
C_{sg}	Lumped stray capacitance to ground
C_{tc}	Turn-to-core capacitance
f_c	Cutoff frequency
i	Current in winding
k_f	Filter cutoff frequency design constant

k_R Filter resistor design constant

K_{sp} Lumped stray parallel capacitance (inter-turn and inter-layer)

K_{tt} Turn-to-turn capacitance

L Inductance

L_f Filter inductor

N Number of turns

R_f Filter inductor's resistance

W_m Magnetic energy

q Electric charge

Introduction

With the arrival of SiC-based switching devices, the switching losses can be considerable decreased in power electronic converters. However, with reduced switching time comes increased voltage rise times.

These high dV/dt values will cause voltage doubling at the connected equipment due to reflections and more capacitive currents will flow in both cables, windings and bearings.

To counter the unwanted effects of fast rise time, passive electrical filters can be employed between the converter and the load. This solution was examined in the project report ([1]) this thesis is based upon, where a LRC-filter was used to dampen overvoltage and rise time.

This report will examine how the filter inductor can be designed to reduce these effects. It is crucial for both the filter performance and the inductor itself that it can withstand high voltage rise times without taking damage and that stray capacitances within the inductor does not affect the filter properties.

Part I

Theory
&
Literature Review

1. Consequences of high dV/dt in windings

1.1 Background

Traditionally, the voltage rise time and the capacitive currents associated with this effect was considered negligible up till the beginning of the 1990s when Pulse-Width Modulation (PWM) motor drives became widespread. Motor drive owners together with inverter- and motor manufacturers discovered that removing the output sine wave filter in PWM-controlled motor drives dramatically impaired winding insulation and bearings. This challenge was circumvented by introducing increased winding insulation, limitations to maximum rate of voltage rise and a number of other measures to reduce the effect of stray capacitances in power cables and connected equipment.

With the introduction of Silicon Carbide (SiC)-devices, these output filters are re-introduced due to increased switching frequencies and shorter rise times. Even though an output sine- or dV/dt-filter greatly decreases the parasitic effects in the power cables and equipment, the input of the filter itself is exposed to the same impacts as the equipment it is protecting.

As mentioned, this report will investigate inductor design to limit these effects. By use of FEM-based computer software, various design parameters such as distance and geometry can be simulated to reveal how parasitic effect change.

First, the theory behind various parasitic effects will be explained.

1.2 Bypassing windings

If the stray capacitance is distributed between turns of the winding, the voltage impulse applied at one end might simply propagate from turn to turn until reaching the opposite winding end [2–4].

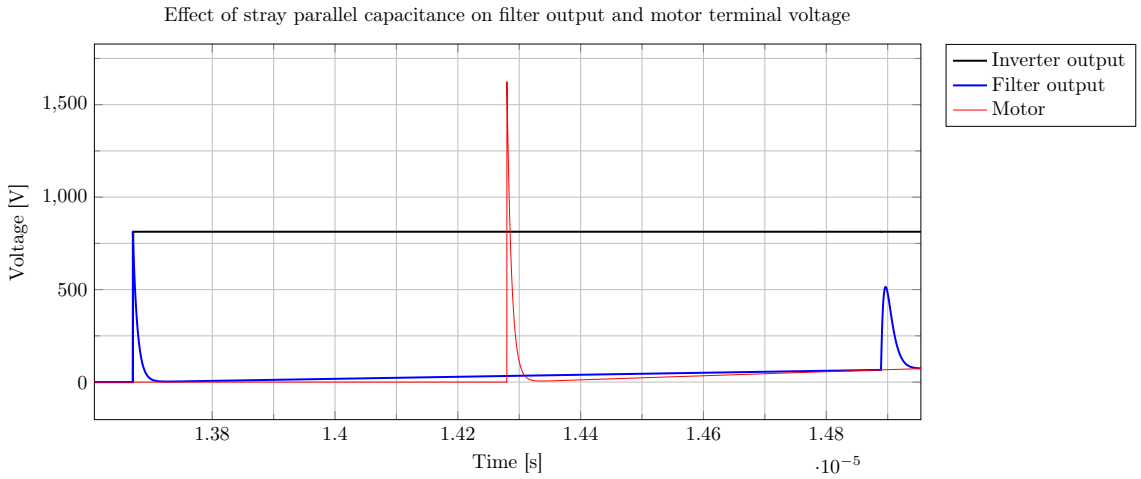

Figure 1.1: Illustration of parallel capacitance and resulting voltage doubling and reflection.

This would effectively circumvent the very purpose of a damping filter inductor as the initial pulse it was supposed to suppress would be outputted at the filter almost instantaneously. This will cause voltage doubling and reflections between connected equipment and the filter output as illustrated in figure 1.1 where the incoming PWM-pulse is outputted immediately and later arrives as a sharp rise pulse at the motor end, causing voltage doubling. The third spike is the reflection returning to the filter output.

This effect is shown later in the report when the designed inductors are tested in SIMULINK.

1.3 Non-linear voltage distribution

When a winding is exposed to a sudden change of voltage, the *capacitive coupling* between winding and ground and between turns themselves in the winding will start to conduct according to $i_c = C \cdot \frac{dV}{dt}$.

The network of parasitic capacitances are often referred to as a *ladder circuit*, and is illustrated in figure 1.2 together with the winding inductance and the series resistance.

The stray capacitances in series within the winding are treated differently than the capacitances to ground and are therefore given different symbols: K is used for inter-turn capacitances and C for capacitances to ground. Note that there are also effects between turns which are not directly neighboring each other, this effect is less significant and decreases with distance. It is therefore neglected in this chapter.

The stray capacitances make the voltage distribution across the length of the winding nonlinear when exposed to sudden voltage impulses, and increases the stress on the first few turns of the insulation [5].

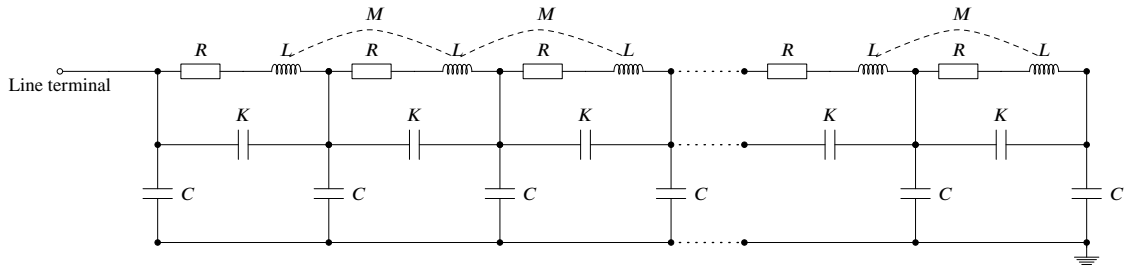

Figure 1.2: The equivalent schematic of a winding, showing parasitic capacitances to ground (C) and along the length of the winding (K), the winding self-inductance (L) and mutual inductance (M) and the series resistance of the conductor (R). One rung in the ladder represents one turn [5].

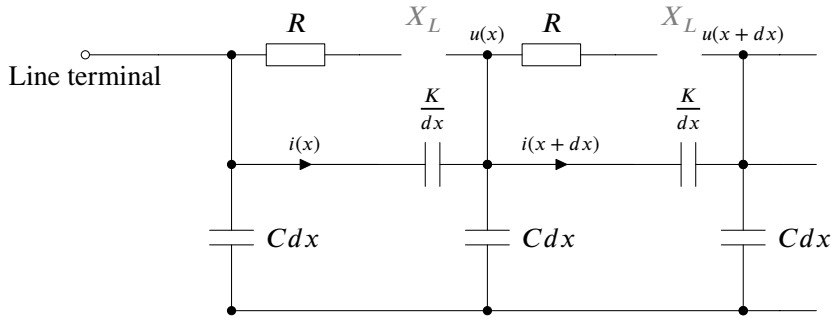

Figure 1.3: The equivalent schematic of a winding exposed to a sudden and significant change of voltage; The winding's reactance, X_L is approximated to an open connection while most of the current will flow in the stray capacitances which will appear like short circuits [5].

In power transformers, which faces many of the same challenges during lightning impulses, the term α is used to describe the linearity of the winding voltage distribution. This term is developed based om the following observations and equations [5]:

During a sudden and significant change of voltage, such as during a switch-on in PWM-modulation, the parasitic capacitances will immediately be charged while the winding inductance appears as an infinite reactance according to:

$$i_C = C \cdot \frac{dV}{dt} \qquad \text{and} \qquad i_L = \frac{1}{L} \cdot \int V \cdot dt$$

The winding network shown in figure 1.2 will then be reduced to a pure capacitance network as illustrated in figure 1.3. By examining an infinitesimal part of the winding, the ground capacitance is denoted as $C \cdot dx$ and the series capacitance as $\frac{K}{dx}$. These now represent stray capacitance per unit length to ground and longitudinal respectively.

Using Kirchhoff's current law:

$$i_k\,(x + dx) + C \cdot dx \cdot \frac{\partial}{\partial t} u(x) = i_k(x) \tag{1.1}$$

where the capacitive current in the longitudinal direction is given as:

$$i_k(x+dx) = -\frac{K}{dx}\frac{\partial}{\partial t}\left[u(x+dx) - u(x)\right] \tag{1.2}$$

When $dx \to 0$, the following is obtained:

$$\frac{\partial i_k}{\partial x} = -C\frac{\partial u}{\partial t} \tag{1.3a}$$

$$i_k = -K\frac{\partial^2 u}{\partial t \partial x} \tag{1.3b}$$

Differentiating (1.3b) with respect to the location x gives:

$$\frac{\partial^3 u}{\partial x^2 \partial t} = \frac{C}{K}\frac{\partial u}{\partial t} \tag{1.4}$$

which can be integrated with respect to time and yield:

$$\frac{\partial^2 u}{\partial x^2} = \frac{C}{K}u + u(x,0) \tag{1.5}$$

where $u(x,0)$ is the voltage distribution relative to ground potential at $t = 0$, which is zero:

$$\frac{\partial^2 u}{\partial x^2} = \frac{C}{K}u \tag{1.6}$$

The general solution to (1.5) can be written as:

$$u(x) = A\sinh(\alpha x) + B\cosh(\alpha x), \qquad \alpha = \sqrt{\frac{C}{K}} \tag{1.7}$$

where α is a factor based on the relationship between longitudinal capacitance along the winding and capacitance to ground.

It is now possible to deduce two equations for the voltage as function of winding length (ℓ). If the far end of the winding is grounded, the end-voltage will always be zero. The voltage distribution between the terminal input and the end is given as:

$$u(x) = U\frac{\sinh\left[\alpha\left(1-x\right)\right]}{\sinh\left(\alpha\ell\right)} \tag{1.8}$$

The curve of (1.8) for different values of α in figure 1.4b.

If the far end of the winding is open, there will be a reflection:

$$u(x) = U\frac{\cosh\left[\alpha\left(1-x\right)\right]}{\cosh\left(\alpha\ell\right)} \tag{1.9}$$

The curve of (1.9) different values of α in figure 1.4a.

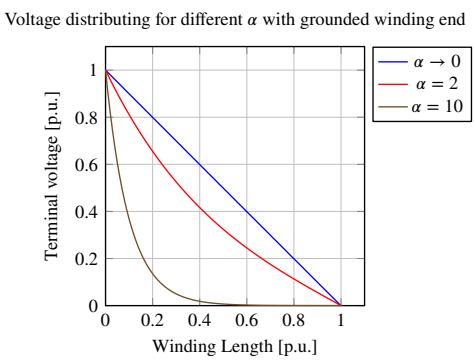

(a) Winding grounded

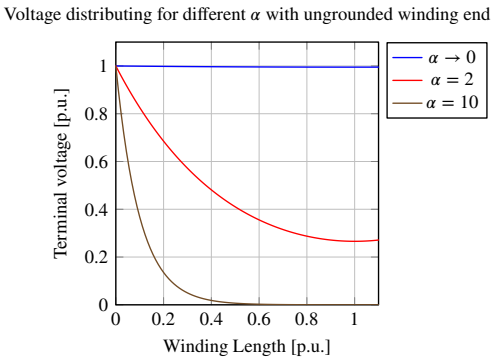

(b) Winding open

Figure 1.4: Voltage distribution as function of winding length for different α for two different winding configurations. [5]

The nonlinear voltage distribution will be applied to the windings later in the report when simulating capacitance between turns and between turns and core.

2. Capacitance

A short review of the theory and properties of the capacitor follows to give context to the focus on stray capacitance in windings and inductors.

The basic circuit element capacitor is a component which can store energy in an electric field. Typically, the capacitor is made intentionally for that purpose in a vast majority of circuits, but as will be shown, the capacitor may also form unintentionally between all nearby surfaces which exhibits a difference in instantaneous charge.

The electric field generated between two terminals of a capacitor is given as:

$$\boldsymbol{E} = \frac{q}{\epsilon A} \tag{2.1}$$

where q is the stored charge on the capacitor terminals and $\boldsymbol{E}$ is the generated electric field and ϵ is the *permittivity* of the material(s) between the charged surfaces. Note that $\epsilon = \epsilon_0 \epsilon_r$ where ϵ_0 is the permittivity of vacuum (defined as $\frac{1}{\mu_0 c_0} \approx 8.8542 \times 10^{-12}\,\mathrm{F/m}$) and ϵ_r is the material's relative permittivity. A is the area of the two surfaces (assumed equally sized).

The voltage across a capacitor is given as:

$$V = \boldsymbol{E}d = \frac{qd}{\epsilon A} \tag{2.2}$$

where d the distance between the capacitor terminals. The current flowing into the capacitor terminals can be derived as

$$i_c = q\frac{d}{dt} \tag{2.3a}$$

$$= \left(\frac{\epsilon A}{d}V\right)\frac{d}{dt} \tag{2.3b}$$

$$= \frac{\epsilon A}{d}\frac{dV}{dt} \tag{2.3c}$$

$$= C\frac{dV}{dt} \tag{2.3d}$$

From (2.3c) and (2.3d), the definition for C becomes:

$$C = \frac{\epsilon A}{d} \tag{2.4}$$

The capacitance is thereby proportional with permittivity ϵ and surface area A, while decreasing with distance d.

Integrating (2.3d) with respect to time gives:

$$\int_{-\infty}^{t} i \cdot dt = \int_{-\infty}^{t} C\frac{dV}{dt} \cdot dt$$

$$V = \frac{1}{C}\int_{-\infty}^{t} i \cdot dt \tag{2.5}$$

$$= \frac{1}{C}\int_{0}^{t} i \cdot dt + V(0)$$

where the integration constant $V(0)$ is representing the initial voltage over the capacitor at time $t = 0$. This constant is what gives the capacitor its memory properties.

2.1 Capacitance in windings

An analytical method to determine the self-capacitance of windings with circular cross section was proposed in [6, 7] and has since been verified both experimentally and numerically by means of finite element analysis software in [4].

The procedure is based on a centric core with two or more turns with capacitance between each turn and between turn and core as illustrated in figure 2.1a.

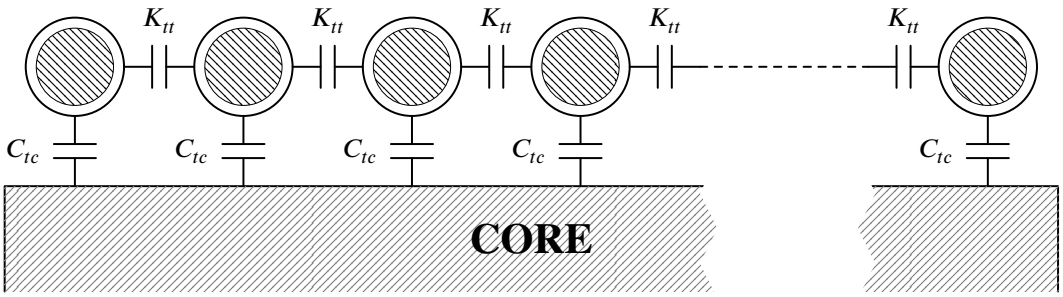

(a) Illustration of circular shaped windings stacked in one layer around a conducting core.

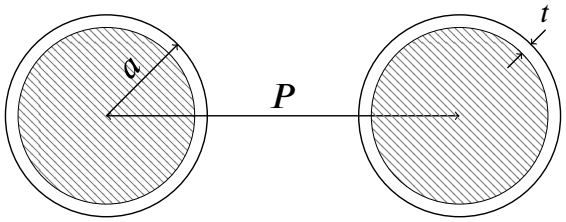

(b) Geometric distances that govern the turn-to-turn capacitance; radius a, center-center distance P and insulation layer thickness t.

Figure 2.1: Winding capacitances between turns and between turns and core. The distances are exaggerated.

2.1.1 Turn to ground capacitance

Assuming that the core is a conducting plane as shown in figure 2.1a, the distance which the electric field line has to travel from conductor to core is half of the distance between two cores [6]. From that we have that

$$C_{tc} = 2K_{tt} \tag{2.6}$$

2.1.2 Turn to turn capacitance

The turn-to-turn capacitance, K_{tt}, when ignoring the insulating layer, can be approximated by

$$K_{tt} = \frac{\pi^2 \epsilon D_T}{\ln\left[\frac{P}{2a} + \sqrt{\left(\frac{P}{2a}\right)^2 - 1}\right]} \tag{2.7a}$$

$$= \frac{\pi \epsilon \ell_T}{\cosh^{-1}\left(\frac{P}{2a}\right)}, \qquad \text{for } t \ll (P - 2a) \tag{2.7b}$$

where P is the center-to-enter distance between each turn, a is the turn radius, t is the thickness of the insulating layer. ϵ is the relative permittivity of the air gap between the turns (figure 2.1b).

For windings with circular turns with diameter D_T, the general equation (2.7a) can be used. For other shapes, i.e. oval, (2.7b) can be used where ℓ_T equals the turn length.

2.1.3 Resulting capacitance

Considering two turns and a core from figure 2.1a, it can be seen that the total capacitance between them consists of a parallel connection of K_{tt} and two C_{tc} in series.

The resulting capacitance between two turns, C_s:

$$C_s(2) = K_{tt} + \frac{2 \cdot K_{tt}}{2} = 2 \cdot K_{tt} \tag{2.8}$$

Increasing the number of turns from two to three, symmetry can be created by splitting the capacitance C_{2c} from the center turn to core in two halves as shown in figure 2.2 and then apply the Δ/Y-transformation [7]:

$$C_s(3) = \frac{K_{tt}}{2} + \frac{C_{tc}}{2} = \frac{K_{tt}}{2} + \frac{2K_{tt}}{2} = \frac{3}{2}K_{tt} \tag{2.9}$$

For four and five turns, the resulting capacitance becomes:

$$C_s(4) = \frac{K_{tt} \cdot C_s(2)}{2 \cdot C_s(2)}K_{tt} = \frac{7}{5}K_{tt} \tag{2.10}$$

$$C_s(5) = \frac{K_{tt} \cdot C_s(3)}{2 \cdot C_s(3)}K_{tt} = \frac{11}{8}K_{tt} \tag{2.11}$$

This can be expanded for n number of turns to

$$C_s(n) = \frac{K_{tt}}{2 + \left(\frac{K_{tt}}{C_s(n-2)}\right)} + K_{tt} \tag{2.12}$$

which builds on $C_s(n-2)$ all the way back to $C_s(2)$ or $C_s(3)$ for even and odd turn numbers respectively. Fortunately, these recursive equations quickly converges to $1.366 \cdot K_{tt}$ as shown in figure 2.3.

It is hereby given that for any winding with more than 8-10 turns, the resulting stray capacitance is only depending on the inter-turn capacitance which is multiplied by that factor.

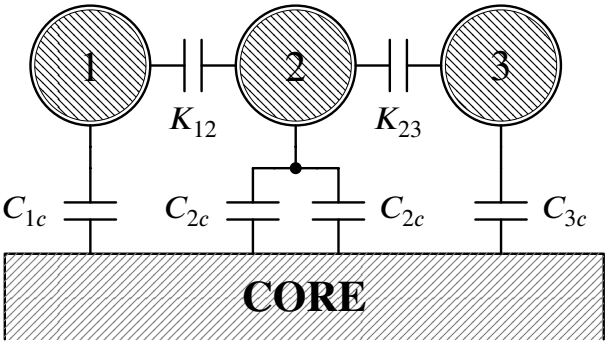

Figure 2.2: Capacitances between turns and core for an odd configuration where symmetry is achieved by splitting the center turn-to-core capacitance into two halves.

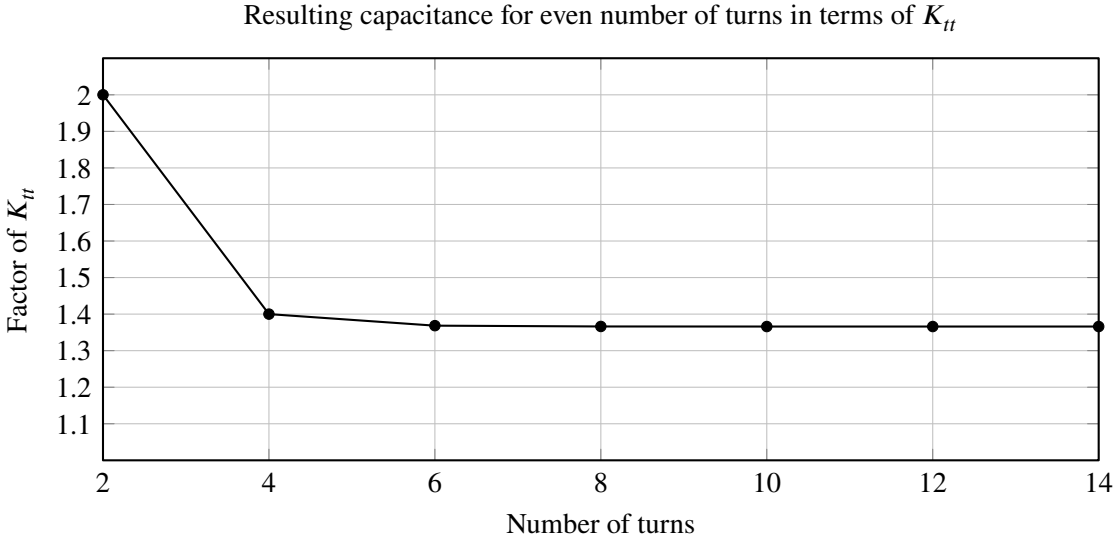

Figure 2.3: The total capacitance of a given number of turns in a single-layer coil quickly converges to $1.366 \cdot K_{tt}$.

3. Magnetic circuits

The inductor's role can be considered as a storage device for magnetic energy in the same way as the capacitor is a storage device for electric energy. Being a magnetic device, it is a part of a magnetic circuit which consists of a *magnetomotive* force ($\mathfrak{F}$), a flux carrying material with a certain *reluctance* ($\mathfrak{R}$) and flux itself (ϕ) [8].

The relationship between those three are often compared to that of Ohm'a law, where the magnetomotive force is seen as the voltage source, the reluctance as resistance and flux as current.

The magnitude of the magnetomotive force is given as:

$$\mathfrak{F} = Ni \tag{3.1}$$

where N is the number of closed loop turns and i the current in the wire.

The magnetomotive force can also be expressed in terms of magnetic flux density $\boldsymbol{B}$, core cross sectional area A and core reluctance $\mathfrak{R}$:

$$\mathfrak{F} = BA\mathfrak{R} \tag{3.2}$$

Remembering how resistance in electrical circuits are defined, the reluctance is similarly given as

$$\mathfrak{R} = \frac{\mathfrak{F}}{\phi} = \frac{l}{\mu A} \tag{3.3}$$

where l is the mean length of the flux carrying material and A its cross sectional area. The term μ is the material's permeability, a property described later in this chapter.

To create a magnetomotive force, a permanent magnet or a current-carrying winding could be inserted into a magnetic circuit. The latter is applied to the flux carrying material by means of one or several turns (N) encircling it (figure 3.1).

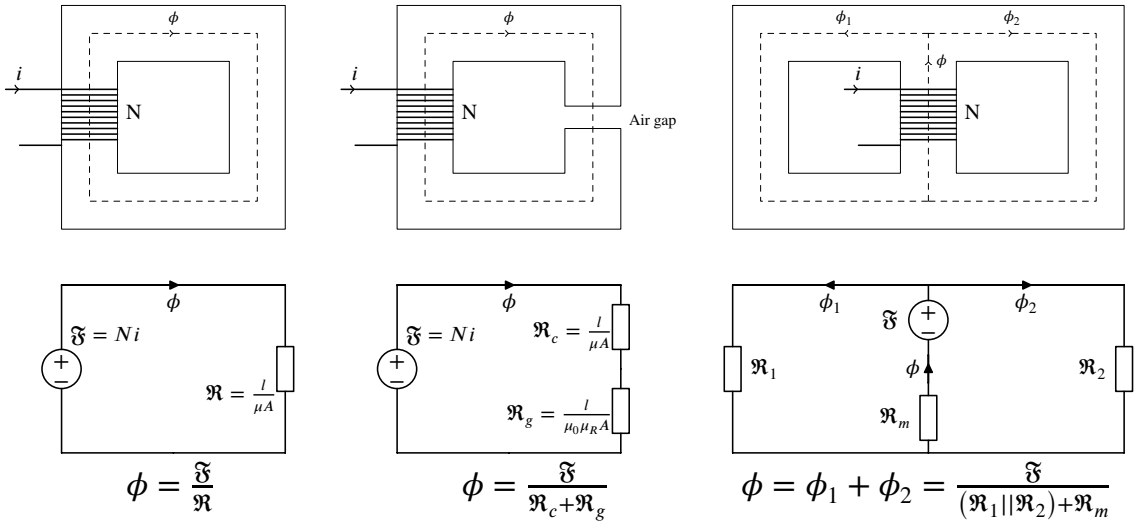

Figure 3.1: Three examples of physical magnetic circuits with their respective electrical circuit equivalent shown underneath.

The free and circulating current i, with density $\boldsymbol{J}$ [A/m^2], will set up a circulating magnetic field with intensity $\boldsymbol{H}$ [A/m] according to Ampère's circuital law:

$$\oint_c \boldsymbol{H} \cdot dl = \int_S \boldsymbol{J} \cdot d\boldsymbol{S} \tag{3.4}$$

The above line integral of curve c is enclosing a surface $\boldsymbol{S}$ which the current density $\boldsymbol{J}$ is passing through. It is important to note that only *free current* will contribute to the $\boldsymbol{H}$-field, regardless of the flux carrying material [9].

Depending on the material's relative permeability, μ_r (which is a result of *bound currents*), a magnetic field with density $\boldsymbol{B}$ will cause a flux, ϕ, to start flowing in a way analogous to that of an electrical circuit (figure 3.1):

$$\phi_s = \int_s \boldsymbol{B} \cdot d\boldsymbol{S} \tag{3.5}$$

where $\boldsymbol{B}$ is the magnetic flux flowing through the surface. If this surface is closed, the resulting net flux has to be zero:

$$\oint_s \boldsymbol{B} \cdot d\boldsymbol{S} = 0 \tag{3.6}$$

From this follows that each flux line, and magnetic circuit, is closed.

3.1 Static magnetic fields

It is also possible to define magnetic flux density in terms of forces and charge. The below equation describes the flux density caused by a charge Q_1 and its velocity $\boldsymbol{v}_1$:

$$\boldsymbol{B} = \frac{\mu_0}{4\pi} \frac{Q_1 \boldsymbol{v}_1 \times \hat{\boldsymbol{R}}}{R^2} \tag{3.7}$$

where R and $\hat{\boldsymbol{R}}$ is the distance and speed of the charge respectively from the point of observation.

This magnetic field is established to explain the force $\boldsymbol{F}$ that that will act on two moving charges in a vacuum:

$$\boldsymbol{F} = Q_1 \boldsymbol{v}_1 \times \left(\frac{\mu_0}{4\pi} \frac{Q_2 \boldsymbol{v}_2 \times \hat{\boldsymbol{R}}}{R^2} \right) \tag{3.8}$$

where $\boldsymbol{v}_1$ and $\boldsymbol{v}_2$ are the speed of the two charges in space. This force is analogous to Coulomb's law which electrostatics are built upon.

Inserting (3.7) into (3.8):

$$\boldsymbol{F} = Q_1 \boldsymbol{v}_1 \times \boldsymbol{B} \tag{3.9}$$

In reality, single charges are rarely treated, so instead a superposition of a multitude of charges are applied:

$$\boldsymbol{B} = \frac{\mu_0}{4\pi} \frac{\sum_{i=1}^{m} Q_i \boldsymbol{v}_i \times \hat{\boldsymbol{R}}_i}{R_i^2} \tag{3.10}$$

However, it is somewhat impractical to know all charges' velocity and direction compared to the direction and magnitude of current. Therefore, the approximation of current density inside the volume is applied:

$$\boldsymbol{J}\, dv = \sum_{i=1}^{m} Q_i \boldsymbol{v}_i \tag{3.11}$$

where m is all the charges in a given volume v.

When observing from a distance R, which is much greater than the internal distance between the charges:

$$\boldsymbol{B} = \frac{\mu_0}{4\pi} \frac{\sum_{i=1}^{m} Q_i \boldsymbol{v}_i \times \hat{\boldsymbol{R}}_i}{R_i^2} = \frac{\mu_0}{4\pi} \frac{\boldsymbol{J}\, dv \times \hat{\boldsymbol{R}}}{R^2} \tag{3.12}$$

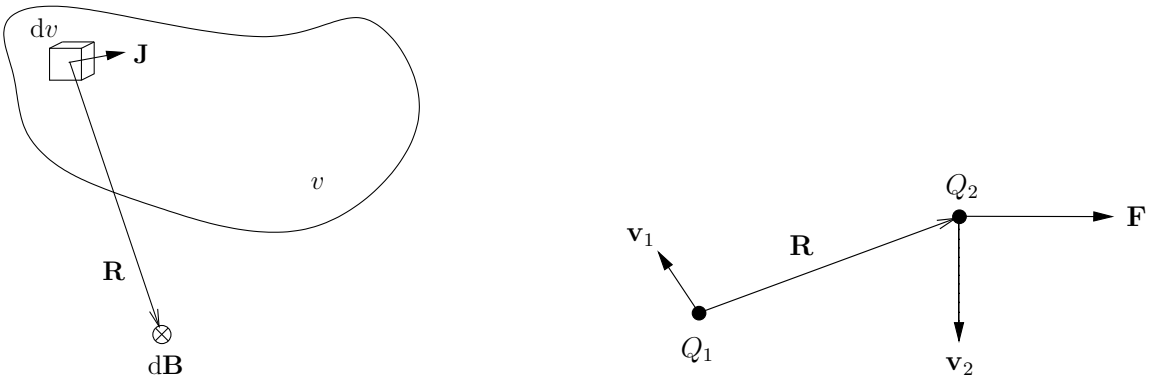

(a) Magnetic flux density $\boldsymbol{B}$ as a result from $\boldsymbol{J}dv$

(b) Two charges with charge Q and velocity $\boldsymbol{v}$ and the resulting force F

Figure 3.2: Relationships between current and magnetic fields [9].

The above equation returns the magnetic field density caused by the current volume $\boldsymbol{J}dv$ which are often referred to as the *current element*. For several current elements enclosed within a volume, the total magnetic flux is given as:

$$\boldsymbol{B} = \frac{\mu_0}{4\pi} \int_v \frac{\boldsymbol{J}dv \times \hat{\boldsymbol{R}}}{R^2} \tag{3.13}$$

This is illustrated in 3.2a

The relationship between any given current, free or bound, and the resulting magnetic field is given by the Biot-Savart law as:

$$\boldsymbol{B} = \frac{\mu_0}{4\pi} \oint_S \frac{\boldsymbol{J} \cdot d\boldsymbol{S} \times \hat{\boldsymbol{R}}}{|R^2|} \tag{3.14}$$

which is a closed line integral over the surface C enclosing a current density $\boldsymbol{J}$ the area of the differential element $d\boldsymbol{S}$ in the direction of the unit vector $\hat{\boldsymbol{R}}$. R is the distance from the wire the magnetic field is observed at. This is illustrated in figure 3.3a.

If the current density is flowing in a wire, this can be approximated to a line integral:

$$\boldsymbol{J} \cdot dv = \boldsymbol{J} \cdot dSdl = JdSd\boldsymbol{l} = Id\boldsymbol{l} \tag{3.15}$$

It is now possible to replace the current element $\boldsymbol{J}$ in (3.14) with $\boldsymbol{I}$:

$$\boldsymbol{B} = \frac{\mu_0}{4\pi} \oint_l \frac{\boldsymbol{I} \cdot d\boldsymbol{l} \times \hat{\boldsymbol{R}}}{|R^2|} \tag{3.16}$$

The relationship between a magnetic field and the resulting flux ϕ is given by Ampere's law as

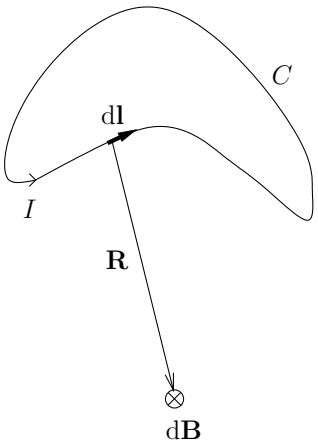

(a) Magnetic flux density $\boldsymbol{B}$ from a line C of current I.

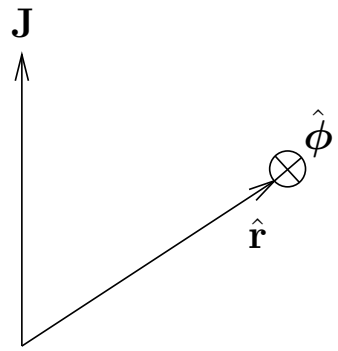

(b) A spherical coordinate system showing a current density $\boldsymbol{J}$ in the $\hat{\boldsymbol{z}}$-direction. According to Biot-Savart's law, the resulting magnetic field $\boldsymbol{B}$ will flow in the $\hat{\boldsymbol{\phi}}$-direction due to $\boldsymbol{J} \times \hat{r}$ in (3.14).

Figure 3.3: Relationships between current and magnetic fields [9].

$$\oint \boldsymbol{H} \cdot dl = \int_S \boldsymbol{J} \cdot d\boldsymbol{S} \tag{3.17}$$

where a closed line integral, which encircles a circulating current density $\boldsymbol{J}$, of the magnetic field intensity $\boldsymbol{H}$ equals the sum of current. It is important to note that only actual free current will contribute to the $\boldsymbol{H}$-field, regardless of the flux carrying material.

The above mentioned magnetic field strength, $\boldsymbol{B}$ relates to the field intensity $\boldsymbol{H}$ by the material constant μ_r, which is a relative factor that denotes the material's magnetic properties relative to that of vacuum. It is also dependent on the *magnetization* $\boldsymbol{M}$ of the material, i.e. the degree of which the magnetic dipoles in the material is aligned and their direction.

$$\boldsymbol{B} = \mu(\boldsymbol{H} + \boldsymbol{M}) \tag{3.18}$$

where $\boldsymbol{B}$ is measured in Tesla (T) or the SI-units $\mathrm{Wb/m^2}$ which can be interpreted as the number of flux lines which crosses a given surface, i.e. flux lines per area. This relationship states that the magnetic field intensity is the same across different materials surrounding a magnetomotive force, but the magnetic field strength varies with the material's magnetization $\boldsymbol{M}$ and its relative permeability.

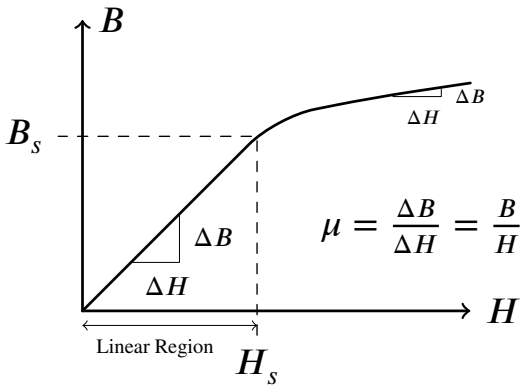

Figure 3.4: The relationship between H-fields and B-fields for a non-linear magnetic material.

$\boldsymbol{M}$ is given as:

$$\boldsymbol{M} = \chi_m \boldsymbol{H} = \mu_0 \left(1 + \chi_m\right) \boldsymbol{H} = \mu_0 \mu_r \boldsymbol{H} = \mu \boldsymbol{H} \tag{3.19}$$

where χ_m is referred to as *magnetic susceptibility* defined as $\mu_r = 1 + \chi_m$
From (3.19) it is seen that μ is given as:

$$\mu = \mu_0 \left(1 + \chi_m\right) = \mu_0 \mu_r \tag{3.20}$$

where μ_0 is a constant and equals the permeability of vacuum: $4\pi \times 10^{-7}$ H/m and μ_r is a unit less factor that spans from 1.0 (vacuum, and approximately 1 for air and most non-ferro magnetic materials) to the order of thousands for different types of ferro magnetic materials such as iron.

As seen in (3.18), the relationship between $\boldsymbol{H}$ and $\boldsymbol{B}$ is linear as long as μ is constant and the material is de-magnetized. The former is true for most non-magnetic materials and for magnetic materials which is far from their *saturation limit*, i.e. in the linear region of the $\boldsymbol{H}\,\boldsymbol{B}$-curve. This curve is seen in figure 3.4.

3.2 Self-Inductance

Considering a closed loop of current surrounded by linear materials, the current i will produce a magnetic field $\boldsymbol{B}$. If the current in the closed loop changes, the magnetic field will subsequently change - thus changing the magnetic flux ϕ through the closed loop. This will induce an electromotive force ϵ, which also will try to change the current. This phenomenon is referred to as *self-inductance* and is defined as

$$L = \frac{\phi}{i} \tag{3.21}$$

As one of the main objectives of this thesis is to design a low parasitic capacitance inductor, knowing how inductance is formed is key. Following the trail from magnetic circuits, a general formula for self-inductance can be found:

$$N\phi = Li \tag{3.22a}$$

$$L = \frac{N\Phi}{i} \tag{3.22b}$$

inserting (3.1) into (3.3) it can be seen that

$$\phi = \frac{Ni}{\mathfrak{R}} \tag{3.23}$$

(3.22b) and (3.23) can then be rewritten as

$$L = \frac{N}{i}\frac{Ni}{\mathfrak{R}} = \frac{N^2}{\mathfrak{R}} \tag{3.24}$$

This equation is used when estimating the required dimensions of the iron core and winding when designing an inductor with a given inductance value.

However, this method does not consider saturation of the magnetic material, leakage flux and other non-linear effects. With that in mind, the *energy method* can be more accurate.

$$W_m = \frac{1}{2}Li^2 \tag{3.25a}$$

$$L = \frac{2W_m}{i^2} \tag{3.25b}$$

where W_m equals the magnetic energy which is linked to the current carrying conductor.

This method requires knowledge of the magnetic energy inside the iron core and gaps, which can be expressed as the vector product of the magnetic flux density vector $\boldsymbol{B}$ and the magnetic field strength vector $\boldsymbol{H}$:

$$W_m = \int_V \left(\int_0^B \boldsymbol{H} \cdot d\boldsymbol{B} \right) \cdot dV \tag{3.26a}$$

$$= \int_V \left(\int_0^T \boldsymbol{H} \cdot \frac{\partial \boldsymbol{B}}{\partial t} dt \right) \cdot dV \tag{3.26b}$$

The energy method is widely used in FEM applications such as COMSOL Multiphysics™.

In section 7.1, the two methods are compared; numerical calculations in COMSOL based on the energy method vs. the analytical approach.

4. Design of inductor

4.1 Introduction

The inductor is in many cases referred to as a magnetic storing device. The property of storing a magnetic field can be taken advantage of in a vast variety of areas, such as in electric machines where the magnetic field is used to transfer energy through air from a stationary part to a moving part. Another example is electric fences where an inductor is used to store energy over time before releasing it to create an instantaneous voltage spike.

It means that when a filter designer requires inductance, what he really requires is means of storing magnetic energy. For filtering applications such as the LRC-filter in this thesis, the storage of magnetic field is taking advantage of the effect an increase of magnetic energy imposes on electric circuits; resisting change of current.

When the current through an inductor tries to increase, the energy forcing this increase is translated into magnetic energy which in turn is released when the current tries to decrease. This has a filtering effect on the current shape as steep edges are smoothed.

For the case of the LRC-filter portrayed in this thesis (explained in detail in the preceding project report, [1]), the storage capability of the electric field is also taken advantage of by the means of a capacitor.

When utilizing the combined effect of charging both a magnetic and an electric storage device which are tuned in capacity to one another and connected in a certain configuration, a desired filtering property is achieved.

This reports examines how the inductor can be designed to exhibit the desired properties in term of inductance, but also in terms of stray capacitance. When a LC-filter is tuned, the exact value of required capacitance is implemented by the capacitor, so adding unwanted stray capacitance to the equation might impede the desired characteristics of the filter.

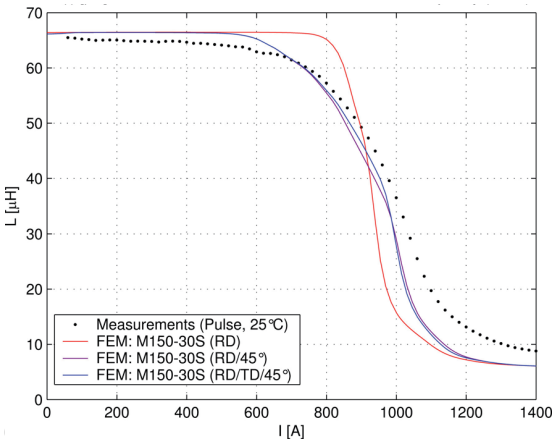

Figure 4.1: Inductance in as function of current in a 60 µH inductance rated for 400 A [10].

4.2 Design considerations

In practice, every current carrying conductor exhibits some degree of inductance by the mere fact that it is establishing a circulating magnetic field according to Biot-Savart's law (3.16). It it thus possible to create inductance by simply adding enough wire and let the inherent inductance suffice. This is also performed in some applications, and if the wire is arranged in a helix like fashion it is referred to as an air-coil inductor.

Inductance is ergo created by having an amount of wire turns that produces a magnetic field forming a closed, magnetic circuit. The strength of the magnetic flux in this circuit indicate about how efficient the inductor is; A high inductance creates more flux at a given number of turns and current according to (3.22b). Further, it was proven in (3.24) that the inductance can be reduced to an equation containing only two terms; turns and reluctance.

It is now understood that the two degrees of freedom available when designing an inductor is the number of turns and the total amount of reluctance in the flux carrying material surrounding the turns.

Ideally, one would therefore design a low-reluctance core to get away with as few turns as possible. Fewer turns means decreased copper losses and also lower losses in the iron as the volume would be very small to accommodate the winding. However, this is not possible due to the non-linear properties of the magnetic materials available today. Depending on the material, the magnetic flux will seize to increase with current between 0.3 – 1.8 T for the most used commercially available materials today [11]. This effect is known as saturation and is an important effect needed to be considered when designing any electro-magnetic device.

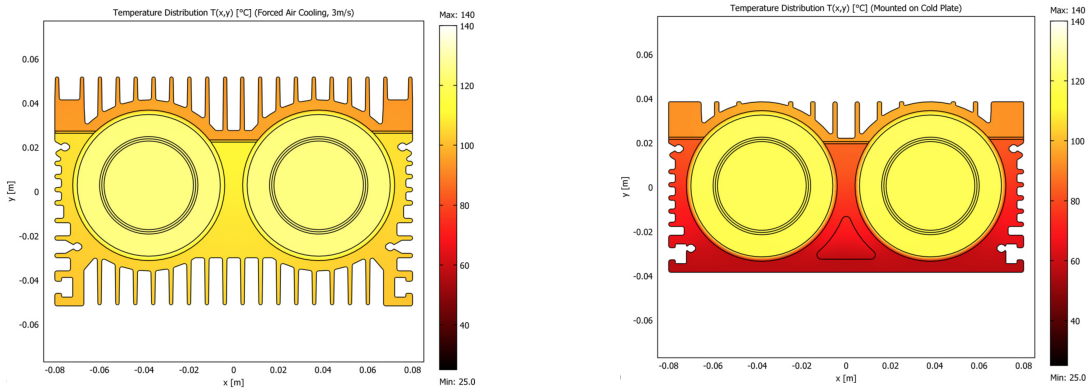

(a) Forced air cooling (air temperature 26 °C) at 3 m/s

(b) Water cooling (water temperature 57 °C)

Figure 4.2: Cross sectional view of temperature distribution for two types of cooling. [13]

When the material saturates, the B-field inside the iron will start to drop towards the relative permeability of air. This causes the reluctance to increase and thus the inductance will drop. This effect is shown in figure 4.1.

This chapter will describe how an inductor can be designed both with regards to the desired inductance as well as with attention to saturation and cooling possibilities.

4.2.1 Cooling

Pockets with trapped, non-circulated air inside the inductor might lead to poor heat transfer due to air's very low thermal conductivity ($0.025\ \frac{\mathrm{W}}{\mathrm{m}\cdot\mathrm{K}}$) compared to copper and iron ($404\ \frac{\mathrm{W}}{\mathrm{m}\cdot\mathrm{K}}$ and $80.4\ \frac{\mathrm{W}}{\mathrm{m}\cdot\mathrm{K}}$ respectively) [12]. It will also be a waste of volume.

When the heat reaches the outer casing, further heat transfer to surroundings is necessary. This can be achieved in several ways; thermal radiation from casing surface to air with subsequent natural convection, forced cooling by the means of fans and mounting on a *cold surface*, i.e. water cooler, with thermal compound. For convection to be more efficient, cooling fins are used.

An example of air-cooled and water-cooled casing design are shown in figure 4.2.

4.3 Inductor design criteria

Since the inceptions of inductors, a vast majority of different types and shapes has been developed, ranging from surface mounted integrated circuits at a few square millimeters to enormous air cored inductors. The size and type of the inductor is mostly based on

application and ratings in addition to special specifications such as build-size and cooling possibilities.

The basis design criteria for the inductor in this thesis will be:

- Applicable for filter applications.
- High current rating; 800 A.
- Small size, should fit inside existing cabinet for a specific marine power converter.
- Inductance value; 212 µH.
- High voltage rating, DC steady state value of 1000 V DC.
- Peak voltage of 120% to 150%.
- One phase per inductor.
- Low stray capacitance.
- Low losses.
- Low thermal resistance to case.
- Low cost.
- Low weight and volume.

It is desirable that a set of three filter inductors can be used in conjunction with a 800 kVA power module, and that these will fit inside the above mentioned cabinet.

4.4 Core design

The high current requirement for this inductor limits the choices of core type. Both in terms of physical winding dimensions and due to magnetic saturation. Traditionally, an inductor of this rating would have been fitted with an E-core, but this type is very bulky. A thorough focus has therefore been placed on a more compact core design. Fortunately, high power drives are equipped with water cooling which provides greater freedom due to the high heat transportation capabilities.

The main purpose of the core is to create a low-reluctance path for the flux to flow out of the winding and return around at the bottom. This reluctance, together with the number of turns, defines the resulting inductance. The reluctance can however not be too low due

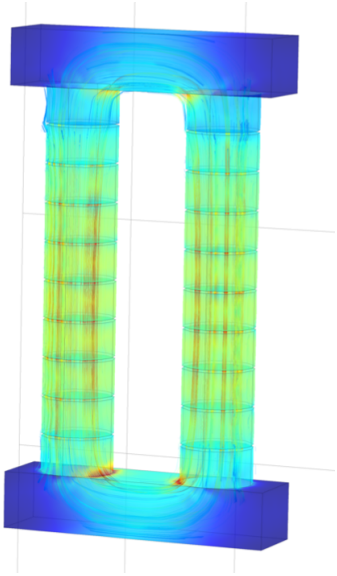

Figure 4.3: Chosen core design; circular legs and rectangular yokes that forms an overall rectangular figure. Here shown with flux lines and flux density in color scale after a FEM-simulation.

Figure 4.4: Different ferrite- and powder core designs (Used with permission from TSC Ferrite International and TSC Pyroferric International).

to the possibility of saturation during current spikes (i.e. short circuits). As a mean to control the reluctance, air-gaps can be introduced in the core material. These air gaps can be designed in three different ways: A single discrete air gap, multiple discrete air gaps in series or as a continuous distributed air gap. Also combinations are possible.

Regardless of type or amount of air gaps, the core shape in this work is chosen to be of rectangular shape, i.e. two long legs with windings and two shorter yokes. The air gap(s) can be inserted in both legs according to required reluctance. This kind of shape has proven usage in other high power inductor types as shown in [10, 14, 15]. Toroid shapes has also been tested in some papers, but due to its bulkiness, this shape is not considered further.

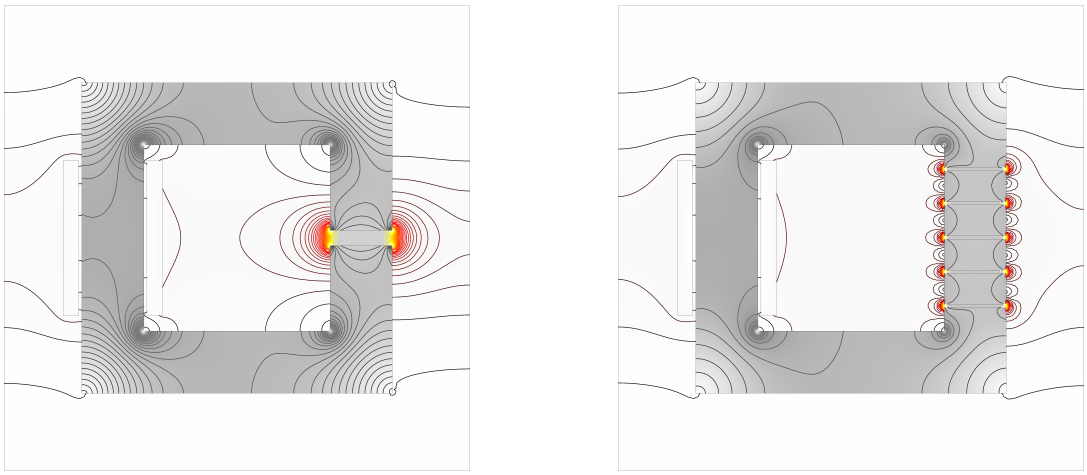

(a) Single 5 mm air gap

(b) Five 1 mm air gaps

Figure 4.5: The difference in B-field fringing from one large discrete air gap compared to several smaller ones with the combined size equal to the single air gap. In this simulation it is also seen that the magnetic energy stored in the single air gap core is approximately 18 % larger than the other. Adding several smaller air gaps thus comes with a cost of added reluctance, but also with the gain of smaller fringing field.

4.4.1 Discrete air gaps

A discrete air gap is made by simply "pausing" the main magnetic material and replacing a given length of the flux path with air. Typically, this air gap is substituted by a different material with the same permeability as air to maintain the structural integrity of the core. The distance can vary from a paper-thin gap to several centimeters, depending on the required core reluctance.

As the distance increases, the magnetic field have a tendency to *fringe* at the gap. The larger the gap, the larger the fringing. This fringed magnetic field might interfere with the surrounding conductors by inducing eddy currents in them. This is undesirable due to the resulting losses.

The effect can be reduced by substituting a single large air gap with several smaller ones in series, albeit with the same total amount of gap distance. This is often referred to as distributed air gap, but in this report it will be referred to as *distributed discrete air gaps* to avoid confusion in the next section.

Figure 4.5 illustrates how the fringing field is reduced when adding several smaller gaps in series instead of a single larger one. Although the combined length of the distributed discrete air gap equals the length of the single discrete air gap, the resultant reluctance is not entirely identical. Simulations performed when creating the figures revealed that the peak flux density in the single gap core was 1.60 T while the peak flux density

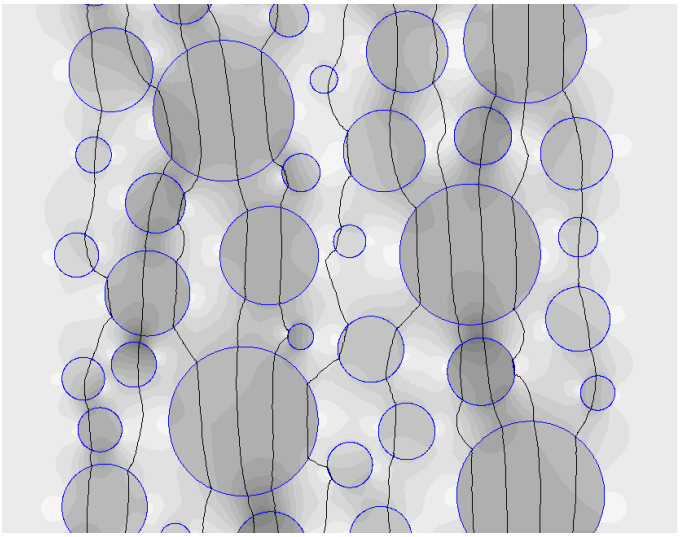

Figure 4.6: Finite-element modeling of a composite structure made of ferromagnetic grains embedded in a non-magnetic matrix. The air gaps between the particles dictate the effective permeability and allow energy storage in magnetic field. The black lines are illustrating the distribution of magnetic flux within the volume of such core. The gray scale shows the resulting flux density (darker color means higher value). Note that the distanced between the particles are deliberately exaggerated for illustrative purposes. *(Image courtesy of S. Zurek, Encyclopedia Magnetica, CC-BY-3.0)*

in the multi gap core was 1.34 T, while the total magnetic energy in the two models were 4.20 J and 3.54 J respectively. This shows that the gain of reducing the fringing flux comes at a cost of lower magnetic energy and thus higher overall reluctance in the magnetic path.

4.4.2 Distributed air gap

This type of air gap is "built-in" inside the iron core material. The core consists of granules in the µm size range made of ferromagnetic particles which individually are coated with a magnetically insulating resin. On a microscopic scale, the flux has to "jump" from granule to granule through the (magnetically) vacuum-like substance between them and through the coating. This is illustrated in figure 4.6. The collective term for this type of material is *powder cores* as the iron particles look like powder before being coated and pressed into the core form. It is important to note that even though these granules are very small, they are still much larger than the magnetic domains which reside inside each granule.

The powder core, with its advantages and drawbacks, will be described in more detail in the following sections.

4.4.3 Core shapes

As illustrated in figure 4.11, a circular shaped core provides the best thermal linkage to the winding and thereby the lowest thermal resistance. Furthermore, the flux linkage between the winding and the iron core will be increased compared to a square shaped core. A higher flux linkage leads to lower leakage fields which again yields more inductance per turn.

To prevent losses from circulating eddy current, the iron core could be laminated. State of the art laser or plasma cutting equipment can produce an approximation to a circular laminated core. This was more impractical or even impossible with earlier manufacturing techniques and square shaped cores was by far the most common in most applications.

Another measure to reduce losses in the core is to add a small amount of silicon (Si), approximately 1 – 7%. This will increase the electric resistance in the material and decrease the circulating current. The trade-off effect is that it will reduce the permeability of the iron.

A third measure is to use a powder core. This type of iron consists of tightly packed bubbles filled with iron or a special alloy, all which are electrically insulated from each other. Eddy currents in these cores are virtually eliminated. Because a powder core can be casted in a mold, a perfect circular shape can be achieved.

The following sections will discuss the various materials with extra attention on powder cores.

4.5 Core material

The core material features many different properties that has to be weighed and considered as there are no universal material available which is perfect for every application.

Properties such as linearity, frequency dependency, eddy current losses, hysteresis losses, Electromagnetic Interference (EMI), magnetostriction[1], saturation level and permeability determines how well a given core type is suited for its application.

According to the list of criteria from section 4.3, low losses is an important property. Also, with the high amount of current involved, low permeability is required to prevent saturation. Low permeability also allows for smaller volume, but due to the high current rating, large windings to accommodate the current will require a certain volume to physically fit the winding, both in terms of turn number and turn diameter.

[1] *Magnetostriction* is a material property which causes the size and volume to change in correlation with the magnetic field direction and magnitude. This causes a audible humming noise with the same frequency as the change in magnetic field direction/magnitude.

Some of the most used types of materials are now presented to provide an overview and basis for material decision.

4.5.1 Laminated steel sheets

Laminations of steel is a well-known magnetic material. It is cheap and features high permeability. When doped with a small amount of silicon (typically in the range of 1 – 7%), it also exhibits relatively low losses. Laminations are employed to reduce eddy currents, but magnetostriction causes a high degree of noise, especially in PWM-applications [16]. Production methods are well established, but due to the finite number of laminations, a perfect circular core is not possible to achieve. This is often approximated to a step-shaped lined circumference that in most applications are acceptable.

Silicon based steel laminations come in thicknesses from typically 0.35 – 0.6 mm and in different grades depending on their desired properties and losses per weight unit.

4.5.2 Amorphous steel

A new type of magnetic material has stretched the idea of laminations even further; amorphous steel consists of laminations at around 0.02 mm and thus the eddy current losses are very low. This type of steel is very brittle and exhibits glass like properties. One example of such amorphous material are manufactured by MetGlas®, but although providing high permeability and low eddy current losses, the magnetostriction is reported to produce extreme noise [10]. The core loss was measured to be 90% lower than typical 3% grain-oriented silicon steel, but the price and the noise would disqualify the material in most inductor applications.

The hysteresis losses in amorphous steel is also very low compared to traditional silicon steel [17].

4.5.3 Nanocrystalline

A tape wound material with extremely low core losses and high permeability. The tape or ribbon thickness can be as low as 10 – 20 µm and the grain size in the range of 10 – 100 nm [18, 19]. This also forms the basis of the material's name.

It was first shown in 1988 when Yoshizawa et. al. added Cu and Nb to an Fe-Si-B alloy [20].

Commercial nanocrystalline cores are available under the names Finemet® (Hitachi Metals), Vitroperm® (Vacuumschmelze), and Nanoperm® (Magnetec), but because of its tape wound structure, it is only in shapes of toroids and beads.

Due to organic content, it suffers from thermal aging of the insulation material [21] and its rated continuous operating temperature is relatively low at around 120 °C. The thermal conductivity is anisotropic, meaning that the heat flux along the laminations are several times higher than between laminations. This makes it challenging to establish an efficient cooling path.

Nanocrystalline was application tested for inductors in [22], where it was concluded with very low losses. However, the paper's focus of application was directed at circuit board mounted miniature inductors, replacing air as magnetic material. Higher current applications were investigated in [23]. As core material for inductors in common mode filters, nanocrystalline showed excellent properties compared to laminated steel, powder iron, ferrites and amorphous materials.

In [24] nanocrystalline is investigated in a 150 kW DC-DC bidirectional converter for (military) hybrid-electric vehicles. The inductor in this application was required to transfer 37.5 kW of power in continuous operation. The size of the inductor, and especially the conductors, were much smaller than what is required for 800 A operation and the inductance itself were about one tenth of what is required in this thesis.

[25] constructed a 25 µH inductor, rated for 25 kW of power in continuous operation and 300 A peak current. Few details are provided about the inductor itself except the inductance (24.2 µH), but based on the wattage it is assumed that also this inductor construction is unsuitable for the requirements in section 4.3.

[26] compares Finemet® and KoolMµ (section 4.5.4) in a 30 kW boost converter application and concludes that the two Kool Mµ-based inductors exhibited lower overall power loss (175 and 214 W) than the nanocrystalline-based inductor (229 W). These are illustrated in figure 4.7. The power loss measurements were conducted in a thermo-anemometer system where all inductors where operating at equilibrium temperature. This result is interesting as the nanocrystalline material according to material properties databases are listed with significantly lower core loss than Kool Mµ. A reason for this result might be that the thermo-anemometer measures the total system loss, not only the core loss.

4.5.4 Powder cores

As mentioned in section 4.4.2, distributed air gaps are often used as a different name for powder cores due to their inherent distribution of miniature air gaps.

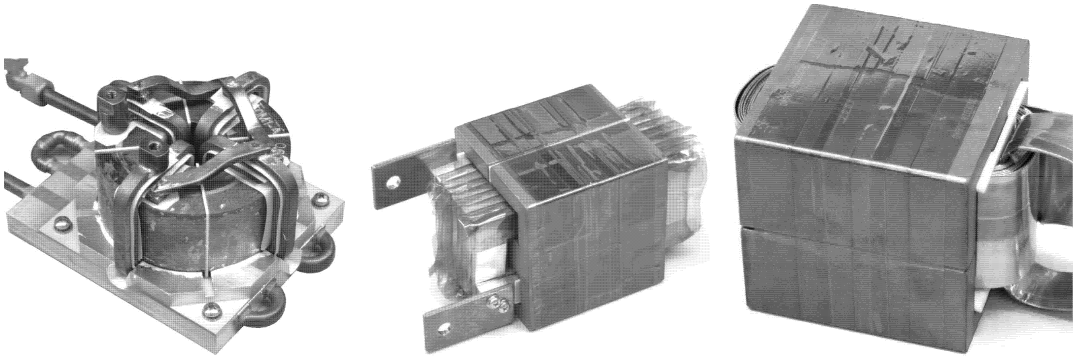

(a) Finemet with toroid core **(b)** KoolMμ with helical winding **(c)** KoolMμ with tape winding

Figure 4.7: The three compared inductor designs from [26], where the total system losses was measured at 229, 214 and 175 W for a, b and c respectively.

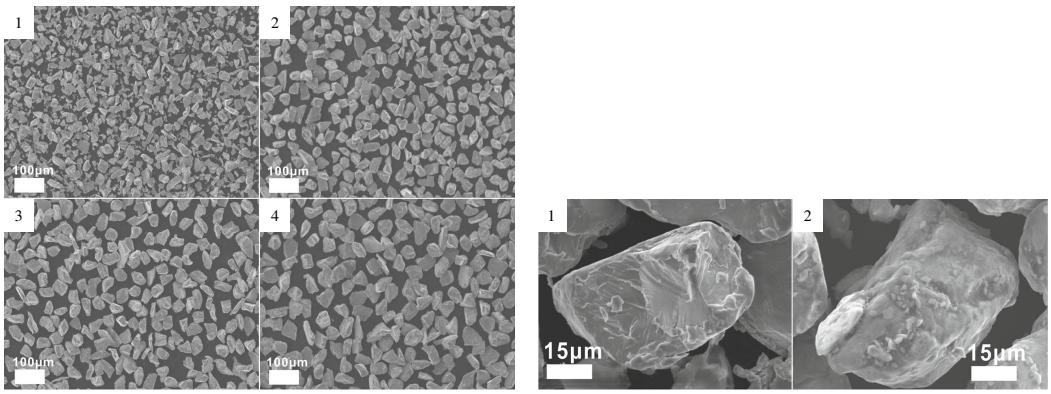

(a) Fe-Si-Al raw powders shown in four different size ranges: 1: ≤ 38 µm.
2: 38 – 45 µm. 3: 45 – 53 µm. 4: ≥ 53 µm.

(b) Raw powder particle (1) and insulated particle (2).

Figure 4.8: Sendust (Fe-Al-Si) powder core as shown from a Scanning Electron Microscope (SEM) [27].

Powder cores come in a vast amount of different types, often with specially designed magnetic properties aimed for certain application such as power factor correction, switch-mode power supplies, harmonic filters etc.

Different types of powder cores and their properties has been studied in [19] [28] and [10] to name a few, but especially [29] has made a thorough and informative comparison. The mentioned papers are used in this report to gain knowledge about advantages and disadvantages of the different powder alloys.

A distinct feature of the powder cores is that the distributed air gap exhibits a strong nonlinear behavior in the BH-curve [10].

Powder cores must not be confused with iron powder, which consist solely of iron. Powder cores are made of an alloy of iron in addition to other materials such as silicon,

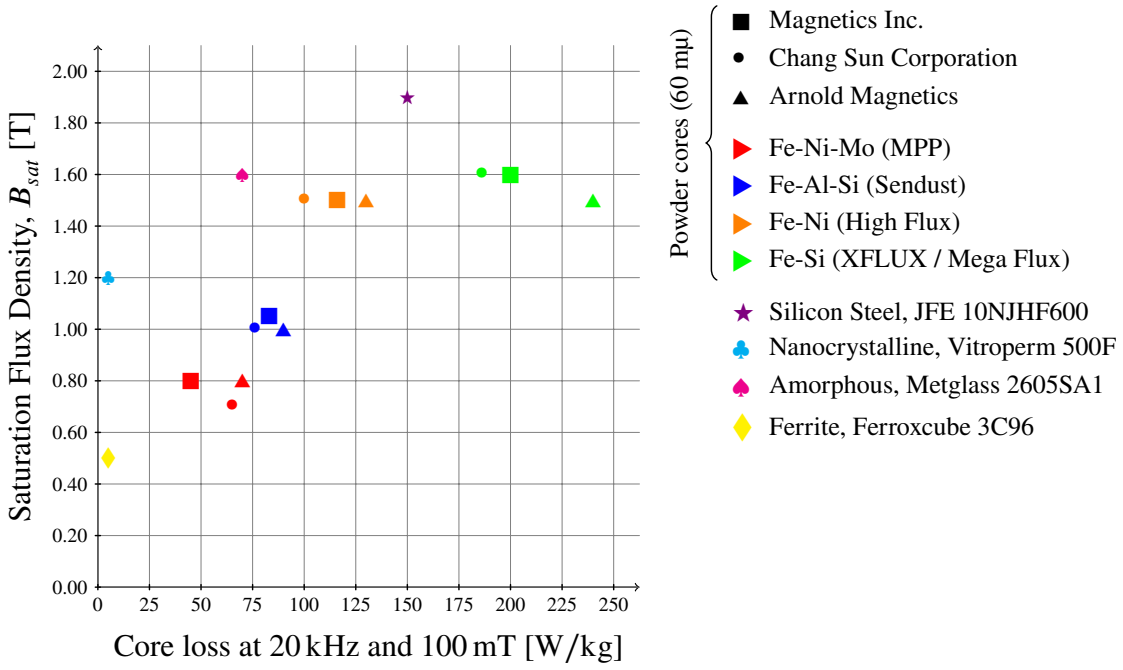

Figure 4.9: A plot of losses as function of rated saturation flux density of a selection of materials from table 4.1. NCD is not included due to loss measurements at different frequency.

aluminum and nickel. There are four main alloy categories, based on the different chemical composition. These are described in the following sections.

Standardized shapes

From the major manufacturers such as Magnetics and Chang Sung Corporation, the following standardized shapes of powder cores are available:

- Toroid
- E-core
- EQ/ER-cores (miniature coils for circuit board mounting)
- U-core
- Segment[2]
- Block (rectangular or cylindrical)

[2] A segment is either a 90° arc length or a straight piece which can be used as building blocks for circular (toroid) or oval ("race track") cores.

Based on the choice of a rectangular core in section 4.4, the powder core should be made of cubical or cylindrical blocks to make the design as compact as possible. It is therefore imperative that the various powder core alloys are available in blocks if the inductor should be assembled.

Fe-Ni-Mo

This alloy is called MolyPermalloy Powder (MPP) and is the powder core which exhibits the lowest core losses amongst powder cores. From table 4.1 it is seen that MPP core loss is 45% and 61% lower than Sendust and High Flux respectively (Magnetics Inc.). Studies show reduction in losses at 32% and 36% compared to Sendust and High-Flux respectively at the same volume, switching frequency and current ripple [30].

Because of the 80% nickel content, this material resides in the higher price range. MPP is currently only available in toroid shapes up to an outer diameter of 165 mm, thus it is not suitable for an inductor in the 800 A size range.

Fe-Al-Si

This material is called Sendust from the area in Japan it was first used; Sendai. Magnetics Inc. and Arnold Magnetics are marketing their sendust powder cores as KoolMμ and MSS respectively. The material has a moderate saturation flux density of about 1 T, low core losses and is available in many geometrical shapes such as toroids, E and U blocks, segments plus square, circular and elliptical blocks from all major manufacturers. Relative permeability is in the range of 14 to 147.

The insulating material does not contain organic materials and it is therefore not affected by thermal aging of the resin. The absence of nickel also makes it cheaper than other powder core alloys such as MPP.

Compared to pure iron powder, the core loss is about 10%, but a negative feature of Sendust is that the core loss increases with temperature. This could cause thermal runaway if the current is large and contributes by external heat flux. It is however possible to adjust the content of of Si and Al to neutralize this effect and even counter-act it by making the temperature dependency negative [31]. Because of this, temperature dependency of core loss in Sendust powder cores is not considered further in this report.

Fe-Ni

Consisting of 50% iron and 50% nickel, this alloy comes with the highest saturation flux density at 1.5 T. It is therefore named *High Flux* by the major manufacturers. The core

loss is somewhat higher than that of Sendust and MPP while the price per volume range is in between the two [32].

It has to be taken into account that with the possibility of higher flux density comes the possibility of reduced core size, so even though the price per volume is in the medium range, the actual cost might be lower when the material quantity is considered.

As with Sendust and MPP, the insulation is not based on organic materials and thus it does not suffer from thermal aging.

In terms of shape, this alloy is only available as toroid from Magnetics and NCD, but Chang Sung Corp. can offer both EQ-cores, U-cores and blocks (rectangular and cylindrical).

Fe-Si

Powdered iron doped with a few percent silicon with high saturation flux density, but which loss wise comes out last of the four mentioned powder types. Available as Mega Flux®from by Chang Sung Corporation and XFLUX®from Magnetics.

The material Crystal-X®from Arnold Magnetics were tested in at least two papers [29, 33] , but no commercial information about the product were found on the producer's web page. Due to the uncertainty of the material's availability and lack of data sheets, Crystal-X is not included in further discussion.

XFLUX®is only available as toroid, while Mega Flux®is available in various type of blocks.

Iron Powder

Pure iron powder is the most cost effective material. However, it comes with higher losses than the previously mentioned powder cores and ferrite cores. The hysteresis losses also make the material's losses increase with frequency such that this material is best suited for low frequency applications where volume is not a key element [34].

4.5.5 Summary of powder cores

The following products are available in block shapes:

- Sendust (Magnetics, Chang Sung Corp, NCD)
- High Flux (Chang Sung Corp.)
- Mega Flux®

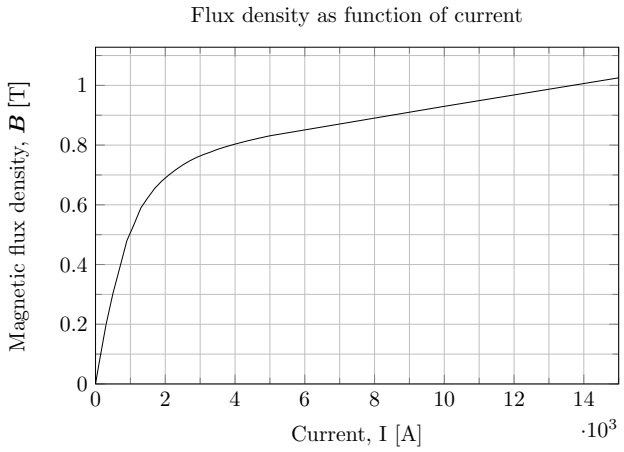

Figure 4.10: The graph shows how the magnetic material start to saturate from the external magnetic field at approximately 1 kA. When the material has fully saturated, it is reduced to the same magnetic properties to that of air. The material used in this simulation was *Alloy Powder Core KoolMμ, 40 mμ*. The relative permeability of 40 means that the first linear part of the curve is 40 times steeper than the last linear part.

From figure 4.9 and table 4.1, it can be seen that from the mentioned materials, the Sendust material from Magnetics (KoolMμ®) has the lowest losses, but also the lowest saturation flux density. The High Flux material from Chang Sung Corp. has twice the loss per volume, but also almost twice the saturation flux density. Due to the high amount of current the inductor should be rated for, it is expected that high saturation flux density is required, but if simulations reveal that there is room to increase the core volume to decrease the flux density, KoolMμ could be considered.

Mega Flux® has about the same saturation flux density as high flux, but with much higher losses.

In terms of cost, Sendust and Fe-Si is generally cheaper than High Flux due to material price [35–37].

Nanocrystalline and Metglass both offers high saturation flux density at low losses, but cannot be used to realize the desired core shape at the time this report is written.

4.6 Saturation

On a molecular level, magnetic materials contain a vast amount of *magnetic domains*, that can be described as tiny magnets with a given orientation. The material's relative permeability indicate how many domains exists per volume unit. When an external magnetic field is applied to the material, these domains start to orient in the same direction as the

external field. This causes the magnetic flux density to increase. This increase is linear when there is a sufficient amount of free domains left to keep the rate of change constant.

However, when the majority of the domains has oriented and fewer and fewer domains are left to turn, the material is said to saturate. When this occur, the magnetic flux density starts to decrease until all of the magnetic domains has oriented into the direction of the magnetic field. When all domains are exhausted, the material remains with the magnetic properties to vacuum, and its relative permeability has been reduced to a value close to unity.

When designing magnetic devices, it is customary to calculate the magnitude of the magnetomotive force the core is expected to endure and the consequent flux density in the core. This is done to dimension the device such that the saturation area of the material is avoided in normal operating conditions.

From the definition of the unit Tesla (Wb/m^2):

$$B = \frac{\phi}{A} \tag{4.1}$$

Revisiting chapter 3, using (3.1) and (3.3):

$$ni = \phi \mathfrak{R}_{tot} \tag{4.2}$$

B can now be expressed in terms of the physical construction of the inductor (core reluctance and turn number) and the amount of current in the winding:

$$B = \frac{\frac{Ni}{l}}{A} = \frac{Ni}{A\mathfrak{R}_{tot}} \tag{4.3}$$

Using $I = I_{max}$ and $B = B_{max} \leq B_{sat}$ it is now possible to check if a given amount of current creates a flux density in the material that causes it to saturate.

4.7 Winding design

In this report, the required inductance is given by the desired filter properties from [1] while the core assembly yields the core reluctance. The amount of turns is thereby given by (3.24). To reduce the length of the core legs, the winding is normally distributed over both legs.

With the amount of turns and general shape of the core given, the following design aspects remains:

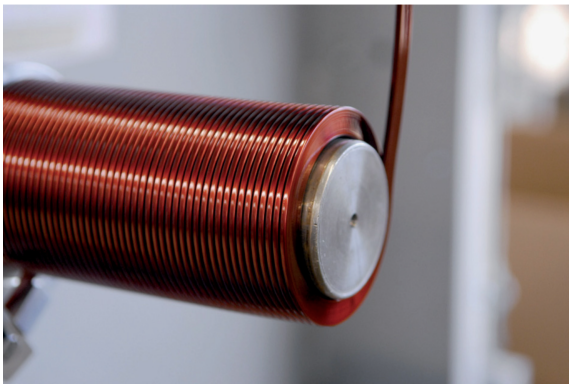

Figure 4.11: Flat helical wire around a circular shaped core. This compact geometry allows for efficient heat transfer due to low thermal resistance. [12]

4.7.1 Winding profile

In terms of cross sectional area, it is decided that the inductor should conduct 800 A in steady state. This requires a cross sectional area of at least 100 mm^2 according to [13] given efficient water cooling with minimum thermal resistance to casing.

In addition to the classical circular winding, two additional conductor shapes are examined in this work; flat helical, vertical helical.

Flat helical profile

The most space saving winding profile is the flat helical as shown in figure 4.11 and 4.12a. This profile is also efficient at transporting heat as it leaves a minimum of air volume given that the core is circular. A possible drawback is the large surface area between winding turns which can give rise to a parasitic capacitance which is unwanted.

A different challenge is that if the core diameter is small, the relative difference in outer and inner radius of the flat helical increases. This can be solved by using individual insulated strands which are pressed in a rectangular manner and interleaved within the conductor boundaries (also known as Litzwire). It is also uncertainty related to how small the bending radius of a 100 mm^2 rectangular copper wire can be and whether or not each turn has to be forged as segments before joining or if a straight conductor can be bent into shape.

Additional challenges with the flat helical profile is fringing flux as reported in [26]. The fringing magnetic flux contribute to losses by inducing unwanted eddy currents in the winding. The authors found that because the flat helical winding occupied a larger volume of the window (see figure 4.7b) it also absorbed a greater portion of the core's fringing flux.

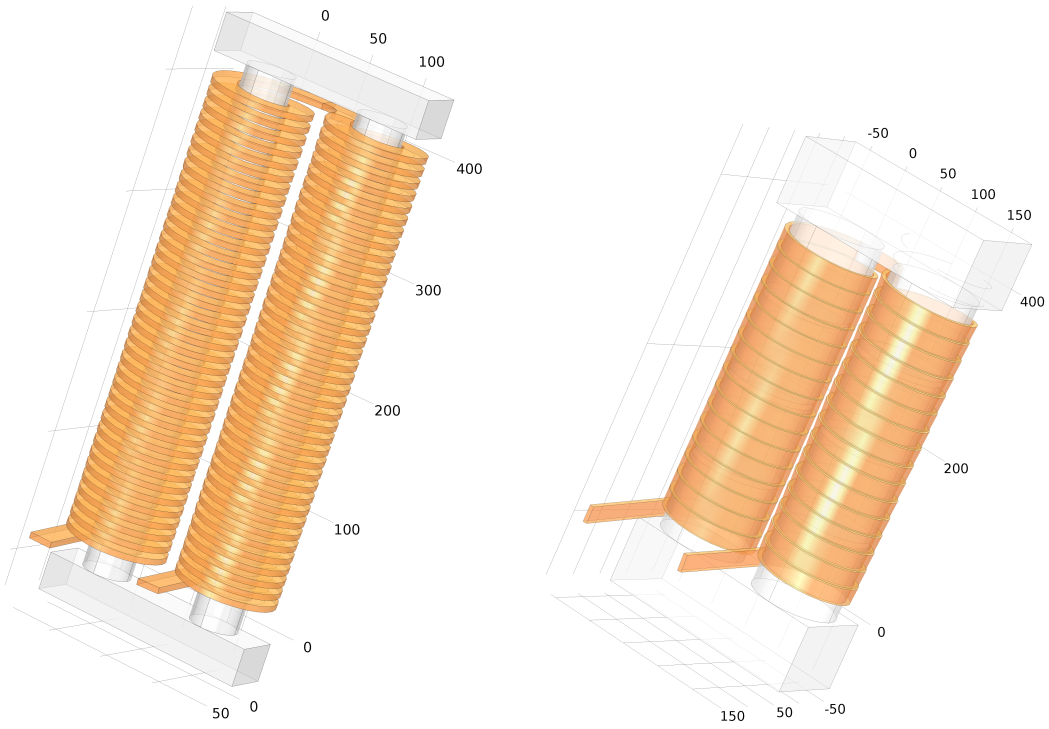

(a) Flat helical; ≈210 µH with 38 turns per leg and core diameter of 40 mm. Conductor is 5 mm high and 20 mm wide.

(b) Vertical helical; ≈220 µH with 16 turns per leg and core diameter of 100 mm. Conductor is 20 mm high and 5 mm wide.

Figure 4.12: Inductor designed to illustrate flat vs vertical helical winding profile, both 100 mm^2. Impact on saturation flux density is not considered in these models.

Vertical helical profile

A rectangular conductor can also be rotated 90° into a vertical stacked turn configuration (figure 4.12b). This approach will increase the required height of the core legs compared to that of flat configuration if the same amount of turns is needed. An alternative to keep the same height is to use fewer turns, but this requires increased core reluctance, either by increasing the length of the discrete air gap(s) or by decreasing the cross sectional area according to (3.3).

Foil winding

Foil windings extend the whole height of the core legs and consists of several turns organized in layers outward from the core. This type of winding is typically suffering from extensive losses from fringing flux [38] and also parasitic capacitance between layers.

4.7.2 Layers

Several layers of turns are an effective way to cut down on core size. Still it comes with some disadvantages which for this work is severe: The most apparent is the severe increase in capacitance between layers as reported in [6, 7, 39].

There is also a problem with heat transport from the core and inner layer to the casing.

Because parasitic capacitance and cooling are the two most important factors in this work, multi-layered inductors are not considered further.

4.7.3 Gaps and fringing effects

Due to magnetic fringing fields near corners of the core, the winding should be kept at a small distance from this area to prevent eddy current losses in the conductors. This also applies close to discrete air gaps, and therefore these gaps should be kept short and distributed over the length of the core leg to minimize the effect.

This issue will mostly affect a vertical helical profile as most of the conductor is very close to the core as opposed to the flat helical conductor where only the inner part is affected.

4.7.4 Winding insulation

To prevent spark-over between turns and between turns and ground, a special type of winding insulation is applied to the wire, usually in the form of lacquer. In this work it is assumed that the insulation will have negligible impact on the main focus points and it will not be included in the models or further discussion, whereas a perfect insulation will be employed.

4.8 Selection of materials and winding design

Based on the above discussion, the following choices are made with regards to core material, core design and winding:

- The core material is chosen to be High Flux due to its high saturation flux density
- The core type is chosen to be of stacked cylindrical blocks as legs and rectangular blocks for yokes.
- The winding profile is undecided, and three profiles will be examined: Flat helical, vertical helical and circular.

Table 4.1: Summary of magnetic materials properties from [29]

Material Type	Manufacturer	Material Name	Chemical Composition	Saturation flux density B_{sat} [T]	Relative Permeability, μ_r	Curie Temperature [°C]	Continuous Operating Temperature [°C]	Core loss at 0.1 T and 20 kHz [kW/m^3][1]
Amorphous	Metglas	2605SA1	Fe-B-Si	1.6	600	395	150[2]	70
Amorphous	Metglas	2605S3A	Fe-B-Cr-Si	1.4	35000	358	150[2]	17
Silicon Steel	JFE	10NJHF600	Fe-Si	1.9	600	700	150[2]	150
Nanocrystalline	Vacuumschmelze	Vitroperm500F	Fe-based	1.2	13200	600	150[2]	5
Ferrite	Ferroxcube	3C93	Mn-Zn	0.5	1800	240	120[2]	5
Powder Iron	Magnetics	Mix-26	Fe	1.4	72	-	140	630
Powder Core	Magnetics	MPP	Fe-Ni-Mo	0.8	14-550	460	<75[3]	45
Powder Core	Chang Sung Corp.	MPP	Fe-Ni-Mo	0.7	26-200	450	200	65
Powder Core	Arnold Magnetics	MPP	Fe-Ni-Mo	0.8	14-350	-	-	70
Powder Core	Ferroxcube	MPP	Fe-Ni-Mo	0.8	14-300	460	200	-
Powder Core	NCD	MPP	Fe-Ni-Mo	0.7	26-160	400	200	240[4]
Powder Core	Magnetics	KoolMμ®	Fe-Al-Si	1.1	26-125	500	200	83
Powder Core	Chang Sung Corp.	Sendust	Fe-Al-Si	1.0	26-125	500	200	76
Powder Core	Arnold Magnetics	MSS®	Fe-Al-Si	1.0	14-147	-	-	90
Powder Core	Ferroxcube	Sendust	Fe-Al-Si	1.0	26-125	500	200	83
Powder Core	NCD	Sendust	Fe-Al-Si	1.0	26-160	600	200	300[4]
Powder Core	Magnetics	High Flux	Fe-Ni	1.5	14-160	500	200	116
Powder Core	Chang Sung Corp.	High Flux	Fe-Ni	1.5	26-160	500	200	100
Powder Core	Arnold Magnetics	High Flux	Fe-Ni	1.5	14-160	-	-	130
Powder Core	Ferroxcube	High Flux	Fe-Ni	1.5	14-160	500	200	-
Powder Core	NCD	High Flux	Fe-Ni	1.5	60-125	500	200	350[4]
Powder Core	Magnetics	XFLUX®	Fe-Si	1.6	26-60	700	200	200
Powder Core	Chang Sung Corp.	Mega Flux®	Fe-Si	1.6	26-90	725	200	186
Powder Core	Arnold Magnetics	Fe-Si 6%	Fe-Si	1.5	14-147	500	200	240
Powder Core	NCD	KFlux®	Fe-Si	1.5	14-147	730	200	650[4]
Powder Core	Arnold Magnetics	Crystal-X[5]	*unknown*	1.5	14-60	-	-	100

[1] 60μ for powder cores,
[2] Limited by lamination epoxy,
[3] Limited by thermal aging,
[4] Measured at 50 kHz,
[5] No further information available

5. Filter design and cable reflections

A short recap of the theory behind passive filter design is provided. Also reflection problems are repeated.

5.1 Filter design

It was found in [1] that the components values of an LRC-filter can be determined using the following algorithm:

1. Compute the wave propagation speed, v, based on cable parameters:

$$v = \frac{1}{\sqrt{L_c C_c}} \tag{5.1}$$

   where L_c and C_c is the cable inductance and capacitance per unit length.

2. Calculate critical rise time, t_{cr}:

$$t_{cr} = \frac{3 \cdot \ell_c \cdot \Gamma_L}{v \cdot 0.2} \tag{5.2}$$

   where ℓ_c is the cable length and Γ_L is the cable load reflection coefficient, often approximated to $\Gamma_L \approx 1$.

3. Determine the cutoff frequency, f_c:

$$f_c = k_F \cdot t_{cr} \tag{5.3}$$

   in [1], k_F the best result was obtained at $k_F = 30$.

4. Calculate filter resistor, R_F, based on cable parameters:

$$R_f = k_R \cdot \sqrt{\frac{L_c}{C_c}} \tag{5.4}$$

where k_R is the filter damping factor. The best performance in [1] had $k_R = 3$.

5. Compute filter inductor value based on cutoff frequency and capacitance:

$$L_f = \frac{R_f}{2 \cdot \zeta \cdot \omega_c} \tag{5.5}$$

where ζ is the relative damping ratio and ω_c is the cutoff frequency given in radians. The relative damping factor was tested in both under-damped ($\zeta < 1$) and critically damped ($\zeta = 1$) conditions in [1]. Under-damped had less filter losses while critically damped had lower voltage overshoot.

6. Determine filter capacitor value based on filter inductance and cutoff frequency:

$$c_f = \frac{1}{L_f \cdot \omega_c^2} \tag{5.6}$$

In this work, the filter inductor's exact inductance is now provided by the COMSOL simulations. Step 5 is therefore omitted in favor for an already known inductance value from [1].

5.2 Reflection

Based on filter- and cable parameters, reflection of voltage waves can occur in fast switching applications.

The propagation time, τ_t, of this wave is given by

$$\tau_t = \ell_c \cdot \sqrt{L_c C_c} \tag{5.7}$$

If the stray capacitance in the filter inductor compromises the filter performance, it is expected to see oscillations occurring at intervals given by this time constant.

Further theory about reflective waves are given in detail in [1].

Part II

Method

6. FEM design

6.1 Introduction

This chapter will describe how the inductor and the different winding profiles is built and tested; by use of FEM-software to develop the inductor parameters and later SIMULINK to test the filter inductor's behaviour.

COMSOL Multiphysics™ is a powerful FEM-based modeling suite capable of calculating multiple physical properties based on CAD-models of devices and structures. In this thesis, COMSOL is employed to calculate electric and magnetic fields involved in the filter inductor. The work in COMSOL is divided into three parts:

1. Build and model an inductor in 3D with a given inductance value. This step is required to obtain an approximate geometry of the inductor core, windings and winding shape which will be used in the next step.

2. Extract a 2D-model of core cross section from the previous step to perform parametric simulations and plot the flux density as function of current.

3. Create a simplified 3D model of the inductor using a single leg and axis symmetry to calculate parasitic capacitance values between turns and to ground.

6.2 Modeling an inductor in COMSOL

This section will describe the steps needed to create and study a 3D-model of an inductor in COMSOL Multiphysics. The steps described are listed in the same order as the natural work flow during the design process:

1. Geometry

2. Materials

3. Physics
4. Mesh
5. Study

6.2.1 Geometry

The filter inductor is modeled in 3D because of its complicated geometry. Further, the model is constructed by extensive use of parameters. This is a time-saving measure to make it easy to adjust i.e. winding size or gap sizes without having to manually re-build and re-position the various part of the CAD-model. Another great benefit by using parameters is that COMSOL is able to iterate over several different values while solving.

The parameter table used for the inductor model is shown in table 6.1. The top part of the table is defined constraints and basic parameters, the middle part is adjustable gap sizes and winding profile while the bottom part is derived values used in the geometrical assembly definitions.

In COMSOL, an additional column exist which evaluates the value and unit of each parameter. This is a helpful aspect of the parameter list while adjusting the parameters prior to simulations. E.g. changing the core radius will automatically update all related parameters with new values, including number of turns required to maintain the given inductance, placement of the windings etc.

Magnetic Core

The first constructed part is two iron core legs which is consists of a number of cylindrical blocks and a given discrete air gap distributed between the blocks. The number of blocks is determined by the number of air gaps which the total discrete air gap is divided into.

For example, a 25 mm total discrete air gap divided into eight gaps makes nine blocks and each air gap would be 3.125 mm (figure 6.1a).

These numbers are used in an array which distributed the iron core blocks into a vertical stack which is the first leg of the inductor. The second leg is mirrored at a given horizontal distance from the first, based on the winding size, gaps and block radius.

The bottom yoke is a rectangular cube with the same cross sectional area as the cylindrical blocks in each leg. Also, the width of the face which couples the yoke and leg together has the same size as the leg diameter. The total yoke length is based on the internal distance between the legs, the width of the winding and the air gap between the core and the winding.

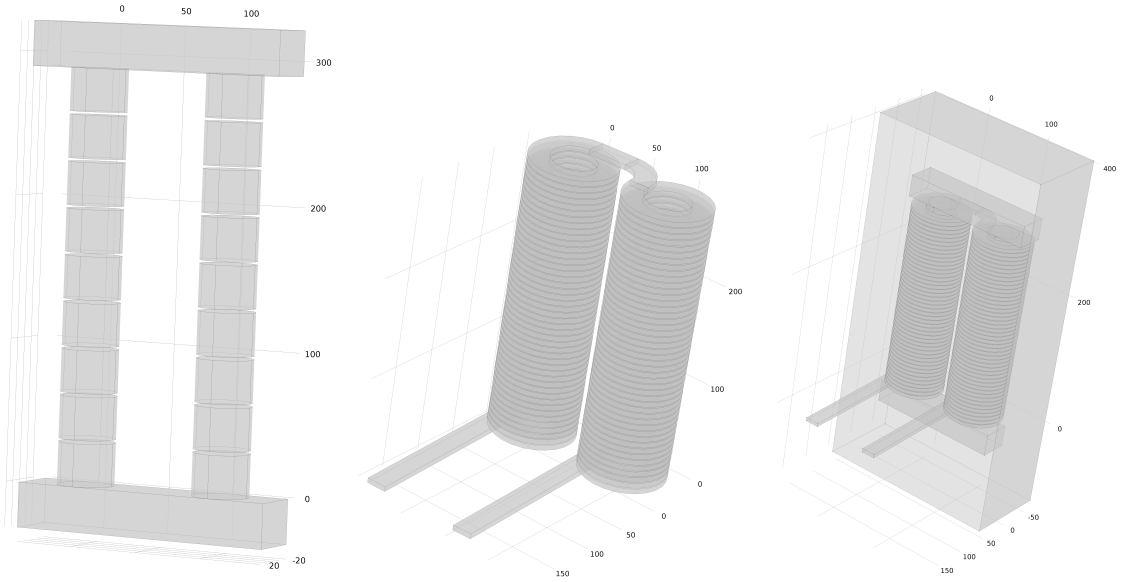

(a) Core **(b)** Winding **(c)** Whole assembly

Figure 6.1: 3D-model of the one of the proposed inductors based on given parameters.

The second yoke is mirrored a given vertical distance away based on the number of core leg blocks and the total discrete air gap length.

Winding

To create the spiral to form the winding, a parametric curve was used. The curve radius is defined by the chosen core radius and the desired gap between core and winding, taking its calculated cross sectional area into account. The curve amplitude as it is spiraling is determined by the desired gap between each turn, taking the desired cross sectional height into account.

As the parametric curve is a one-dimensional, a separate 2D plane was created to act as the cross section of the winding. For a flat helical profile, this plane is a rectangle. The plane is then swept along the parametric curve to create a three-dimensional winding.

Two spirals are created, one for each of the core legs. The number of turns in each winding is determined by the desired inductance after calculating the core's total reluctance using (3.24). The calculated turn number is then rounded and split into the two spirals, one for each leg.

The estimated inductance correlates closely with the simulated inductance which is based on the energy method, typically within a few percent. If the difference in estimated and simulated inductance is too large, the rounding of turn number can be altered form `ceil` to `floor`.

A special connecting geometry is also created to bind the two windings together in a series connection. The size and shape of these parts are based on the existing geometry to automatically adapt when altering the winding shape, core size, gap lengths etc.

FEM-required geometry

For the FEM-simulation to be able to accurately calculate electric and magnetic fields, the model has to be placed in a volume with defined material constants. An air-filled container is therefore created in which the inductor is placed. Furthermore, the input- and output terminals of the inductor has to extend out of this container. This is for the circulating current to be able to "jump" from one terminal to the other and form a closed loop.

It is also possible to define a geometrical domain as *infinite elements domain*. This would make COMSOL treat the boundary of that domain as an infinite volume of i.e. air. As almost all the magnetic field lines are concentrated inside the core material and in close proximity of the discrete air gaps, the infinite element domain is not used as it severely prolongs simulation time.

The discretely defined air container is thought to be sufficiently large to avoid significant inaccuracies due to astray flux lines not being included in the simulations.

6.2.2 Materials

COMSOL features a vast amount of predefined materials which can be applied to the different part of the geometry. Also user-definition of materials is possible by inserting values for the material's constants.

The inductor model consists of three materials: Surrounding air, copper winding and a core of a specified non-linear magnetic material. Winding insulation other than air is not included in this model as its impact on calculated inductance and magnetic fields is assumed insignificant while the added simulation time is considerable.

The non-linear magnetic material features both HB- and BH-curves that can be employed by the boundary conditions to determine saturation of the material. The relative permeability is defined by the user, but some materials are based on a given value from the producer, i.e. 60 mμ for the material *Alloy Powder Core Hiflux 60 mu*.

6.2.3 Physics

The applied physics and boundary conditions is the core of the model in COMSOL. Within the area of this report, the AC/DC-module contains several physics-environments:

- Magnetic Fields
- Magnetic and Electric fields
- Electrical Circuit
- Electric Currents
- Electrostatics

Magnetic and electric fields

This module is chosen for the initial study of the inductor where the main goal is to determine inductance and magnetic flux density in the core.

The basis of Ampère's Law and current conservation is the foundation applied to all parts of the model. The Initial Values-conditions are set to 0 for both magnetic vector potential and electric potentials, i.e. there is no residual flux in the core and the winding is without charge.

A second domain boundary is chosen for the magnetic core where the magnetic field's constitutive relation is set to *HB-curve* to correctly model the saturation in the core.

The winding domain is assigned to the boundary condition *Multi-Turn Coil*, where the coil type is chosen as *numeric* due its custom design. The coil excitation is also configured for current at the amplitude given in the parameters listed in table 6.1.

6.2.4 Mesh

In FEM tools, the mesh is a grid which is distributed across the volumes and surfaces of each model part. The intersections in the mesh defines a coordinate in which a value should be calculated. Mesh sizing is a trade-off between accuracy and simulation time, but can be adjusted with different sizes for different parts.

In this model, the most interesting parts are the core and the winding, thus these two components has mesh size in category *fine*, which is size 4 of 9 different mesh sizes. The default size, *normal*, is size 5. The air volume in the container is less interesting and is therefore designated to level 7, *coarser*. The mesh is illustrated in figure 6.2.

6.2.5 Study

This part determines how the simulation is conducted and how the equations are solved. In this report, the *frequency domain*-study is used for 3D-models, while a *stationary* study is performed for the parametric sweeps in the 2D-models.

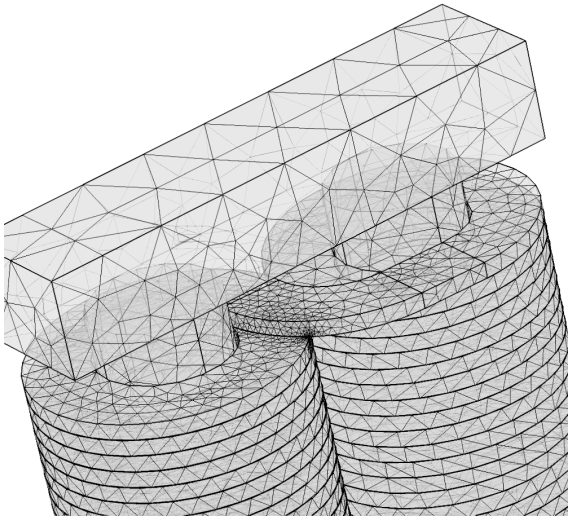

Figure 6.2: Close-up of the surface mesh of the flat helical inductor 3D-model.

To prepare the numeric coil for simulation, a special study named *coil geometry analysis* is required prior to the main study.

The Newton-Raphson iteration method is employed together with the SSOR and FGMRES-solvers and is configured with a maximum permissible error in estimate of 0.0010.

6.3 Proposed designs

To evaluate the impact different conductor profile has stray capacitance, three different inductors will be made:

- Model-1: Flat helical winding
- Model-2: Vertical helical winding
- Model-3: Circular helical winding

The 3D-models will be connected to an 800 A current source in the *magnetic and electric fields*-physics environment in COMSOL. This value is chosen as it is the maximum steady state RMS current according to the inductor design objectives listed in section 4.3.

Three 2D-models should also be designed as cross sections of their respective 3D-model. These will be used for parametric simulations to calculate flux density in the core as function of current from 100 – 3000 A in 100 A steps.

Table 6.1: Model parameters for 3D inductor model

Name	Expression	Description
I	800 [A]	Test current
freq	1 [kHz]	Frequency
L_wanted	212 [uH]	Wanted inductance
Mu_r_core	16	Iron core permeability
A_wire	100 [mm^2]	Conductor cross section area
R_core	20 [mm]	Iron core radius
H_segment	30 [mm]	Height of one core section
N_gaps	7	Number of discrete air gaps
Gap_air_tot	20 [mm]	Total length of discrete air gaps
Gap_turn	1 [mm]	Air gap between helical turns
Gap_topbottom	10 [mm]+4*Gap_turn	Air gap between yokes and winding
Gap_core	2 [mm]	Air gap between core and turns
Gap_helis	20 [mm]	Air gap between winding 1 and 2
Flat_y	5 [mm]	Height of flat helical winding
Flat_x	A_wire/Flat_y 2*R_core+2*Gap_core+Gap_helis	Flat helical winding width
l_mean	+2*((N_gaps+1)*H_segment+Gap_air_tot) +2*((pi*R_core^2)/(2*R_core))	Mean length of flux path
R_air_tot	Gap_air_tot/(mu0_const*pi*R_core^2)	Reluctance of discrete air gap
R_iron	(l_mean-Gap_air_tot) /(Mu_r_core*mu0_const*pi*R_core^2)	Core reluctance
Pitch_flat	Gap_turn+Flat_y	CC distance between flat turns
A_yoke	pi*R_core^2	Area of iron core yoke and legs
R_flat	R_core+Flat_x/2+Gap_core	Helix radius for flat conductor
R_wire	sqrt(A_wire/pi)	Conductor radius
N_needed	sqrt(L_wanted*(R_air_tot+R_iron))	Required turns to obtain wanted L
N	ceil(N_needed/2)	Rounded number of turns per yoke
L_estimated	(N*2)^2/(R_air_tot+R_iron)[uH]	Estimated inductance
B_max_est	(N*2*I)/(R_core^2*pi*(R_air_tot+R_iron))	Estimated max flux in the core

7. Numerical vs. analytical calculations

FEM-calculations are numerical by nature and their accuracy are depending on mesh resolution and solver specifications, herein factors in error estimates, damping factors and iteration method.

In this report, the Newton-Raphson iteration method is employed with a specified error estimate of 0.00010.

As numerical results are difficult to verify, they should be compared to an expected value. Important values are therefore also calculated analytically prior to simulations to serve as guide.

If an analytical and numerical approach are congruent, it is expected that further numerical calculations are true as long as the model is approximately equal.

For example, if numerical and analytical calculations of circular shaped conductors yield the same turn-to-turn capacitance, it is also expected that square-shaped conductors will produce correct numerical results when all other conditions are unchanged.

This assumption takes advantage of the fact that the COMSOL solvers are indifferent to the shapes within the model and performs the same type of calculations regardless of circular or square conductors.

One should however be aware of meshes for circular shapes should be more detailed than square shapes to preserve accuracy.

Three important values are compared with analytical calculations in this report:

1. Inductance
2. Flux density
3. Stray capacitance

7.1 Inductance

Prior to commencing simulations in COMSOL, the parameter list (table 6.1) would auto-update and calculate the given variables. The expected inductance, `L_estimated`, is

founded upon the reluctance (core dimensions, relative permeability and air gaps) together with the number or proposed turns, `N_needed`. This value is based on the desired inductance, `L_wanted` = (212 µH). The estimate is calculated using the analytical formula (3.24):

$$L = \frac{N^2}{\mathfrak{R}} \tag{7.1}$$

COMSOL is using the energy method in a numerical approach (3.26b) to perform these calculations, thus incorporating the complete magnetic energy within the model domain:

$$W_m = \frac{1}{2} L \cdot I^2 \tag{7.2a}$$

$$L = \frac{2 \cdot W_m}{I^2} \tag{7.2b}$$

However, as mentioned in section 3.2, this approach requires knowledge of the magnetic energy inside the iron core and air gaps, W_m. This energy can be expressed as the vector product of the magnetic flux density vector $\boldsymbol{B}$ and the magnetic field strength vector $\boldsymbol{H}$:

These two, along with the current magnitude, I, are known values in COMSOL after a simulation has completed.

The inductance can therefore be calculated by the following equation:

$$L = 2 \cdot \frac{\boldsymbol{B} \times \boldsymbol{H}}{\left(\frac{|I|}{\sqrt{2}}\right)^2} \tag{7.3}$$

The above calculation can be expressed in COMSOL as a *global evaluation* using the following command:

```
(mef.normB*mef.normH*2) / (abs(mef.ICoil_1)/sqrt(2))^2)
```
(7.4)

The variables for field strength/density and current is given as `mef.normB`, `mef.normH` and `mef.ICoil_1` respectively.

7.1.1 Correction factor

When creating and testing the COMSOL models, it was discovered that the FEM-calculated inductance was approximately 10% lower than expected. This is thought to be caused by

Table 7.1: Analytical vs. numerical inductance calculation for flat helical winding

Description	Parameter name	Value
Required inductance	`L_wanted`	212 µH
Core radius	`R_core`	20 mm
Mean length of flux path	`L_mean`	0.696 m
Total discrete air gap length	`Gap_air_tot`	25 mm
Relative permeability of core	`Mu_r_core`	14
Total reluctance (air)	`R_air_tot`	1.58×10^7 H[1]
Total reluctance (core)	`R_iron`	3.04×10^7 H[1]
Required number of turns	`N_needed`	98.96
Adjusted number of turns per leg	`N`	53
Analytically calculated (estimated) inductance	`L_estimated`	243.22 µH
Numerically calculated inductance	-	218.53 µH
Difference between estimated and FEM-calculated		10.28%
Difference between required and FEM-calculated		2.75%

[1] The unit for reluctance is equal to the unit for inductance, although the two concepts are different.

the increased reluctance which is added to cores with several discrete air gaps compared to a single discrete air gap as showed in figure 4.5 and discussed in section 4.4.1.

Consequently, a correction factor of 7% was added to the parameter calculations to upward adjust the number of turns on each leg. This value is tuned to increase the estimated inductance, `L_estimated`, approximately 10% higher than the required inductance and thus counter the effect of multiple discrete air gaps.

With this method incorporated, the numerical and analytical calculations are closely in agreement as seen in table 7.1. Because of the discrete nature of fixed core block dimensions and integer number of turns, it is not always possible to achieve the exact needed inductance.

7.2 Flux density

Knowledge of the flux density is important to avoid designing an inductor which saturates prematurely. An analytical method to estimate the resulting peak flux density is therefore employed in the parameter list based on (3.2):

$$\begin{aligned} \mathfrak{F} &= Ni = BA\mathfrak{R} \\ B &= \frac{Ni}{A\mathfrak{R}} \end{aligned} \tag{7.5}$$

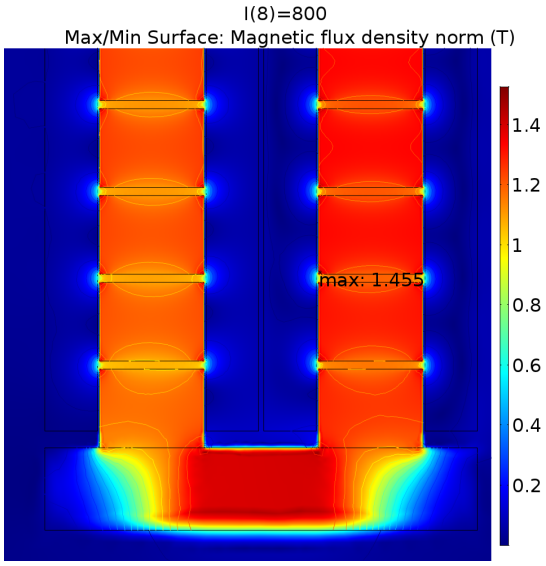

Figure 7.1: A closeup of the magnetic flux density in a 2D cross sectional view of a 3D-model. The point in the model with the highest flux density is marked together with its value.

For a 3D-model with flat helical winding profile identical to the model described in table 7.1 and with test current of 800 A, the resulting peak flux density was analytically calculated to 1.461 T while the 2D cross sectional model of the same geometry yielded a peak flux density at the almost the exact same value: 1.455 T. This is illustrated in figure 7.1.

7.3 Capacitance

A circular shaped winding profile was modeled to verify consistency with the findings about parasitic capacitance calculations presented by Massarini in [6]. The winding consisted of 20 turns of 100 mm^2 conductors around a core with radius 20 mm (figure 7.2).

Geometry and calculations results are presented in table 7.2. The analytical method utilized is presented in section 2.1, and equation (2.7b) is repeated for convenience:

$$C_{tt} = \frac{\pi \epsilon \ell_T}{\cosh^{-1}\left(\frac{P}{2a}\right)}, \qquad \text{for } t \ll (P - 2a) \tag{7.6}$$

As seen from table 7.2, the results from FEM-calculations are not too far off the analytical approach and is therefore accepted. Note that COMSOL is not able to derive a complete lumped series capacitance, so that the recursive equation (2.12) is again employed, i.e:

$$C_{tot} = 1.366 \cdot C_{tt} \tag{7.7}$$

Table 7.2: Analytical vs. numerical capacitance calculation of circular conductor

Description	Parameter name	Value
Conductor area	`A_wire`	100 mm^2
Conductor radius	`R_wire`	5.64 mm
Gap between turns	`Gap_turn`	0.5 mm
Gap between winding and core	`Gap_core`	0.5 mm
Core radius	`R_core`	20 mm
Center-to-center distance	`p`	11.78 mm
Winding circumference	`l_t`	164.25 mm
Analytical turn-to-turn capacitance	`c_tt`	15.40 pF
Numeric turn-to-turn capacitance	-	14.23 pF
Total lumped capacitance (based on numeric result)	`c_tot`	19.44 pF
Difference between analytical and FEM-calculated		7.59%

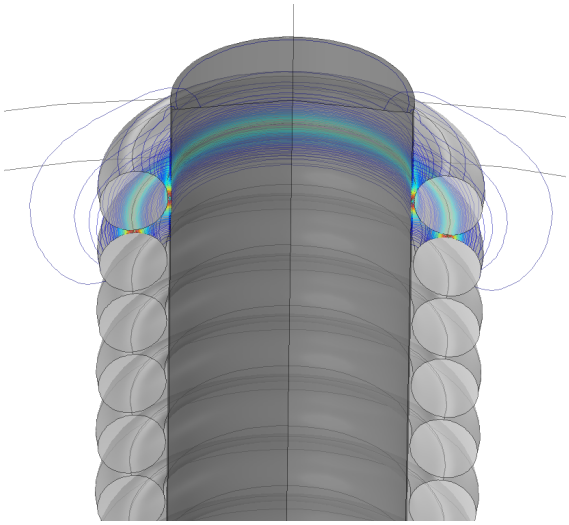

Figure 7.2: A closeup of the electric fields in a 2D axisymmetric model used to calculate stray capacitance between windings.

when the number of turns are > 10.

7.4 Per-unit base values

The following base units are used in the result section.

They are based on a 800 kVA inverter unit with a nominal voltage at 1000 V DC and nominal current of 800 A. Nominal fundamental frequency is 60 Hz.

Base impedance:

$$Z_{base} = \frac{V^2}{VA} = \frac{690^2}{800 \cdot 10^3} = 0.595 \tag{7.8}$$

Base frequency:

$$\omega_{base} = 2\pi f = 2\pi 60 = 376.99\,\text{rad/s} \tag{7.9}$$

Base inductance:

$$L_{base} = \frac{Z_{base}}{\omega_{base}} = \frac{0.595}{376.99} = 1.578\,\text{mH} \tag{7.10}$$

Base capacitance:

$$C_{base} = \frac{1}{Z_{base}\omega_{base}} = \frac{1}{0.595 \cdot 376.99} = 4.458\,\text{mF} \tag{7.11}$$

8. Inductor testing in SIMULINK

During the preceding project work from last semester, the filter inductor tested in SIMULINK was an ideal inductor with no stray capacitance or resistance.

After the inductor and winding designs have been model and simulated in COMSOL during the work in this report, their values are inserted in the SIMULINK model during testing on filter performance. This will provide more accurate results and reveal how the stray components are affecting the filter behavior.

8.0.1 Stray capacitance in parallel

The lumped stray capacitance will be connected in parallel with the inductor and the winding's DC resistance in series.

It was found in the project report [1] that a cutoff frequency of 27.4 kHz in combination with a damping resistor of 59.4 Ω had the best filter performance in terms of losses and minimum voltage overshoot.

The LRC-filter's cutoff frequency will remain at 27.4 kHz, but because the three inductors modeled in COMSOL has different inductance, the filter will have a slightly different filter capacitance in each case according to (5.6).

The filter resistor will be adjusted according to the internal DC-resistance of the inductor winding to avoid excess losses.

The filter topology together with inverter, cable and load is illustrated in figure 8.1 and the SIMULINK model in figure 8.2.

8.0.2 Stray capacitance to ground

The inductor core is assumed insulated from ground due to the insulated coating of the powder granules inside the core. Stray capacitance to ground is thereby depending on external elements such as the filter's distance to the inverter and how the cabling is coupled to ground. Also the filter cabinet and inductor casing contribute to stray capacitance.

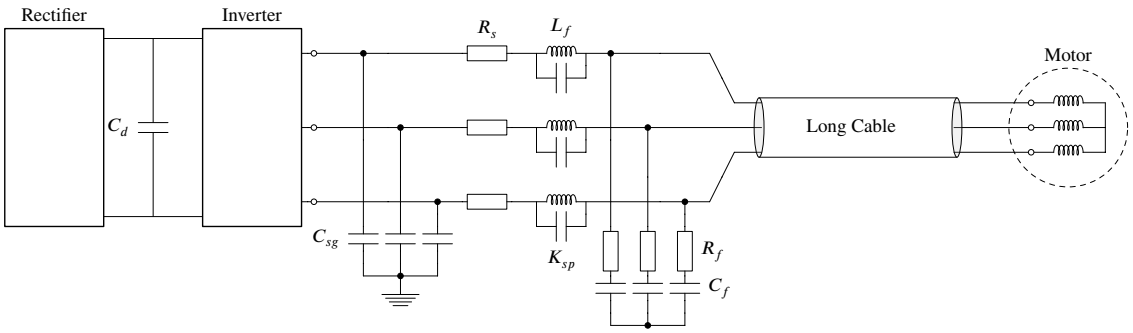

Figure 8.1: Experimental SIMULINK model of the complete LRC-filter with lumped, stray capacitance in parallel, K_{sp} and to ground, C_{sg}

It is difficult to estimate these values, so a modest value of 1 pF is used. Increasing this value improves the filter performance in terms of reflections, but also requires more current from the inverter.

In a realization of this filter, capacitance to ground should therefore be designed such that desired filter performance is achieved with the minimal amount of "wasted" current from the inverter to ground. Excessive current "wasted" on stray elements to ground can cause higher components cost on the inverter side to accommodate this current, and is unwanted.

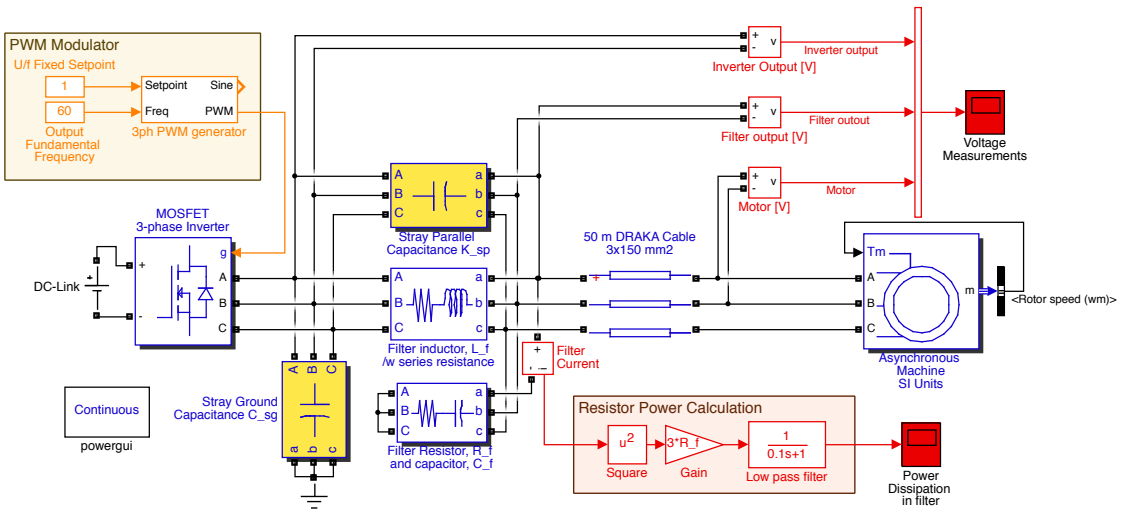

Figure 8.2: The SIMULINK-model from [1] is expanded to contain stray capacitances, highlighted in yellow. Measurements are in red, and the main electric circuit is in blue. More details about the model are found in appendix A

Part III

Results and discussion

9. Proposed inductor designs

The proposed inductor designs are presented in table 9.1 and illustrated in figure 9.1.

9.1 Model-1: Flat helical inductor

With a core cross section of 25 mm and winding height of 5 mm, this design is very compact and light weight compared to Model-2 and Model-3. Due to the size and geometry of the winding, manufacturing cost are thought to be higher.

The winding should also distribute current evenly so that litzwire might be necessary. This will increase cost compared to a circular conductor or the vertical helical conductor.

The inductor core, winding and complete assembly is presented in figure 9.1.

9.2 Model-2: Vertical helical inductor

The powder core block radius in this model is twice as large as in Model-1: 50 mm vs. 25 mm. This was designed on purpose as the total inductor size would be several meters long using the same block radius with a vertical winding profile.

For the same reason, the peak flux density is estimated to be significantly lower in this model as the cross sectional area is four times larger.

A major drawback of this design is the weight, which is almost six times as heavy as Model-1.

Due to the very narrow discrete air gaps, the estimate according to (3.24) was more accurate and the correction factor was therefore omitted in this model.

Again, the initial design values were used throughout the geometrical design process to construct a revised inductor with core and winding according to table 10.1 and it is illustrated in whole in figure 9.1.

Table 9.1: Dimension and key values for the proposed inductor designs

Parameter	Model-1	Model-2	Model-3	Unit
Number of turns	80	54	72	-
Core relative permeability	14	14	14	-
Number of powder core cylindrical blocks	7x2	20x2	16x2	-
Dimension of powder core blocks (radius x height)	25 x 30	50 x 30	35 x 20	mm
Total length of discrete air gaps	25.00	25.00	25.00	mm
Yoke height	39.27	78.54	54.98	mm
Overall core height	313.54	782.08	614.96	mm
Overall core width	185.00	242.00	185.57	mm
Overall core depth	50.00	100.00	70.00	mm
Total powder core volume	1541.9	8513.7	3275.6	cm^3
Total powder core weight [1]	11.37	62.77	24.15	kg
Winding outer diameter	91.50	120.00	96.57	mm
Winding cross section	100	100	100	mm^2
Overall winding length	18 300	20 296	19 935	mm
Total winding volume	1830.0	2029.6	1993.5	cm^3
Total winding weight [2]	16.40	18.19	17.86	kg
Total inductor weight	27.77	80.96	42.01	kg
Outer inductor height	314	782	615	mm
Outer inductor width	185	242	186	mm
Outer inductor depth	92	120	97	mm
Total inductor volume[3]	5344	22 709	11 095	cm^3

[1] Density of powder core 7373 kg/m^3.
[2] Density of copper 8960 kg/m^3.
[3] Given as height x width x depth.

9.3 Model-3: Circular helical inductor

Again it is seen that a non-flat winding at high current amplitude leads to a massive core given that the core material's relative reluctance is unchanged.

The turn number correction factor was reduced to 2.5% in this model as the per-gap length is somewhere in between Model-1 and Model-2.

It also is expected that the winding of this inductor is considerable cheaper than the flat helical winding.

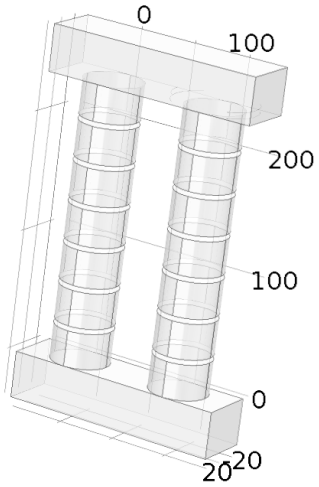

(a) Model-1 Core

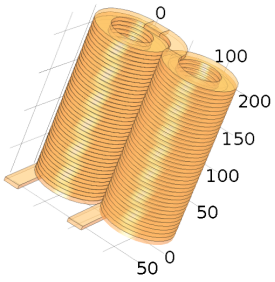

(b) Model-1 Winding

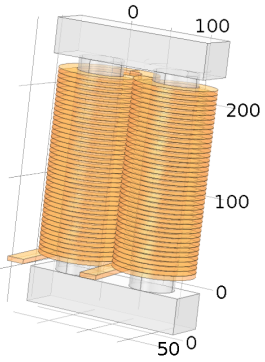

(c) Model-1 Full assembly

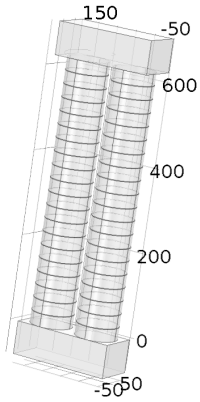

(d) Model-2 Winding

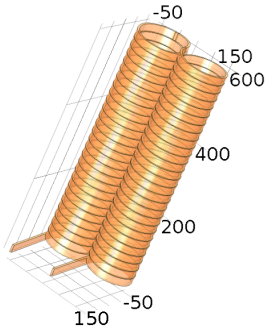

(e) Model-2 Core

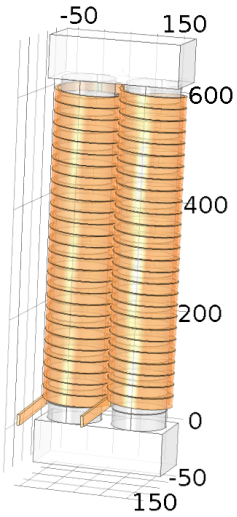

(f) Model-2 Full assembly

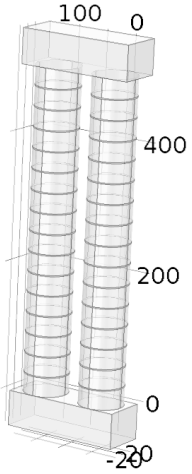

(g) Model-3 Core

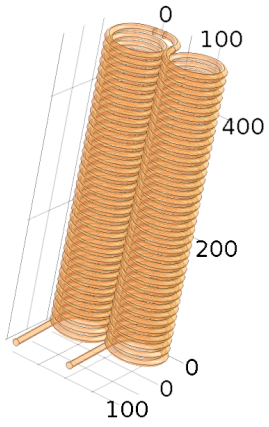

(h) Model-3 Winding

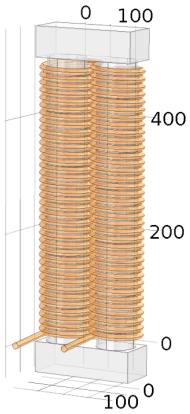

(i) Model-3 Full assembly

Figure 9.1: Proposed designs for the three inductors. Units given in millimeters. Note that the vertical axis starts above the bottom yoke.

10. Inductance and flux density simulations

The following field simulations are carried out on NTNU's supercomputer *Vilje*, running COMSOL 5.2.

Simulation time varied between two and seven hours per model, depending on the number of meshing points.

The coil inductance was found using the built-in feature which calculated all electrical properties of a defined winding. This value was compared with a manually entered equation for the energy method, (7.4), and found equal.

All values are presented in table 10.1.

10.1 Model-1: Flat helical inductor

The total coil inductance was found to be 211.9 µH. This is very close to the required inductance. The filter performance for this inductor and its parasitic capacitance will be tested in SIMULINK and is presented in the following chapters.

The estimated peak flux density was founded on geometrical considerations and was evaluated in the parameter table which both the 3D and 2D-model is based upon. The analytically calculated estimate is very close to the numerical result which was extracted from the two dimensional cross section model (figure 10.1).

During the parametric sweep with test current from 100 – 3000 A, the peak flux density was calculated and is plotted in figure 10.2. The first version of this model had a core radius 5 mm less then the current model, and the flux density at rated current was too far into the saturated region (1.46 T). By increasing the core radius, the flux density decreased to 1.21 T which is at the top of the linear region (figure 10.2).

If practical experiments reveal that linearity is needed at higher current level, e.g. short term over load, the core cross section should be increased, or the length of the discrete air gaps can be increased.

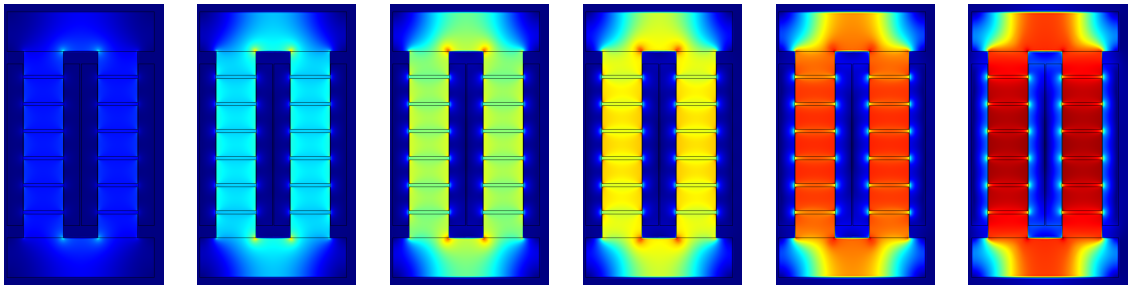

(a) 200 A 0.38 T | **(b)** 500 A 0.90 T | **(c)** 800 A 1.21 T | **(d)** 1000 A 1.29 T | **(e)** 1700 A 1.39 T | **(f)** 3000 A 1.49 T

Figure 10.1: Flux density shown with color scale for the 2D of flat helical inductor. The values indicate the applied test current and resulting flux density in the core. The measurement is taken in the right leg, vertically centered and horizontally towards the core window.

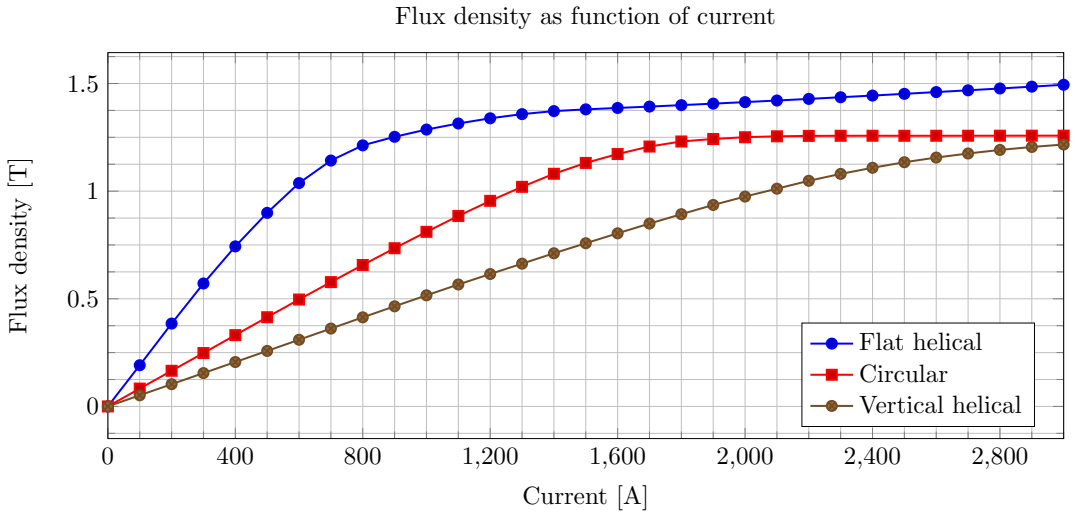

Figure 10.2: Graph showing flux density as function of current. The measurement is taken midway in the right core leg.

10.2 Model-2: Vertical helical inductor

The total coil inductance was found to be 216.76 µH. Which is slightly higher than the required inductance. The effect on the filter will be tested in SIMULINK together with the calculated stray capacitance.

The most apparent disadvantage of this the design is the large core volume which is more than five times larger than that of the flat helical inductor, and 2.5 times longer.

Due to the large cross sectional area of the core, the flux density is also considerable lower. During the parametric sweep with test current from 100 – 3000 A, the peak flux

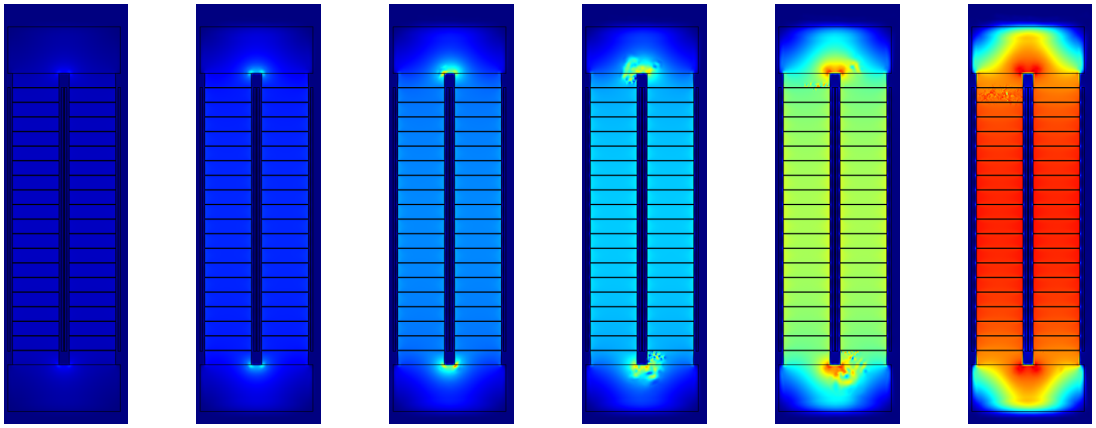

(a) 200 A 0.10 T | **(b)** 500 A 0.26 T | **(c)** 800 A 0.41 T | **(d)** 1000 A 0.52 T | **(e)** 1700 A 0.85 T | **(f)** 3000 A 1.22 T

Figure 10.3: Flux density shown with color scale for the 2D of vertical helical inductor. The values indicate the applied test current and resulting flux density in the core. The measurement is taken in the right leg, vertically centered and horizontally towards the core window.

density was calculated and is shown plotted in figure (figure 10.3). It is seen that the core does not saturate until about 2800 A.

10.3 Model-3: Circular helical inductor

The total coil inductance was simulated to be 215.5 µH which is in the same region as the two former simulations. Again, the core dimensions are considerable larger than Model-1 but far from the extreme volume of Model-2. The winding length is approximately the same. Overall, this design is a trade-off between Model-1 and Model-2 in most aspects.

The flux density starts to saturate at about 1800 A which is well beyond rated current (figure 10.4 and table 10.1).

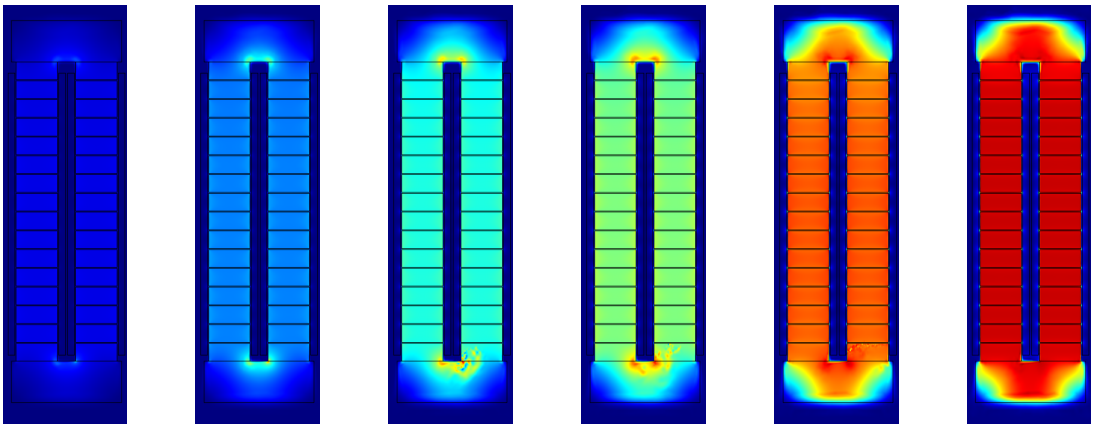

(a) 200 A 0.17 T | **(b)** 500 A 0.41 T | **(c)** 800 A 0.66 T | **(d)** 1000 A 0.81 T | **(e)** 1700 A 1.21 T | **(f)** 3000 A 1.26 T

Figure 10.4: Flux density shown with color scale for the 2D of circular helical inductor. The values indicate the applied test current and resulting flux density in the core. The measurement is taken in the right leg, vertically centered and horizontally towards the core window.

Table 10.1: Design and calculation results

Parameter	Model-1	Model-2	Model-3	Unit
Target inductance	212.0	212.0	212.0	µH
Estimated inductance [1]	214.6	218.5	223.1	µH
Calculated inductance	211.9	216.8	215.5	µH
Calculated inductance	0.134	0.137	0.137	per-unit
Estimated flux density	1.21	0.412	0.661	T
Calculated flux density [2]	1.21	0.413	0.660	T
Calculated lumped capacitance [3]	542.6	216.7	70.7	pF
Calculated lumped capacitance	121.71×10^{-9}	48.61×10^{-9}	15.86×10^{-9}	per-unit
Series resistance	3.1	3.4	3.3	mΩ

[1] Adjusted for discrete air gap energy loss with 7% in Model-1 and 5% in Model-3.
[2] At 800 A, measured in right side core leg.
[3] Calculated with turn-to-core distance 0.1 mm and turn-to-turn distance 0.1 mm.

11. Capacitance simulations

Using the geometry achieved in the 3D-model, a separate 2D axis-symmetric model was built for each of the three winding profiles.

In these models, the physics interface *electrostatics* was used to calculate the capacitance matrices between turns. Each model consists of 20 individual discs which were designated as a *terminals*. The voltage applied to each terminal is according to (1.8).

Two types of simulations are conducted; with a grounded and conducting core and with the core insulated. Each simulation iterates over two parameters; turn-to-turn distance and turn-to-gap distance.

To maintain axis symmetry, only one core leg i modeled and the yoke is left out. There are consequently no magnetic fields involved in these simulations. The air gaps in the core were also omitted as the core itself turned out to have very little effect on the resulting capacitance.

The three models are shown in figure 11.1.

Some initial results are already revealed in table 10.1 where lumped parasitic capacitance are shown for the different winding profiles. These results are calculated at minimal distance between winding and core and between turns; 0.1 mm.

This chapter will explore how capacitance are affected by distance and conductor shape. In total 600 different simulations were conducted:

- parametric sweeps increasing both winding-to-core distance and turn-to-turn distance independently from 0.1 to 1.0 mm in steps of 0.1 mm.
- These 100 simulations were performed with and without a conducting core and repeated for all three designs.

11.1 Results

Three main observations were made during the simulations:

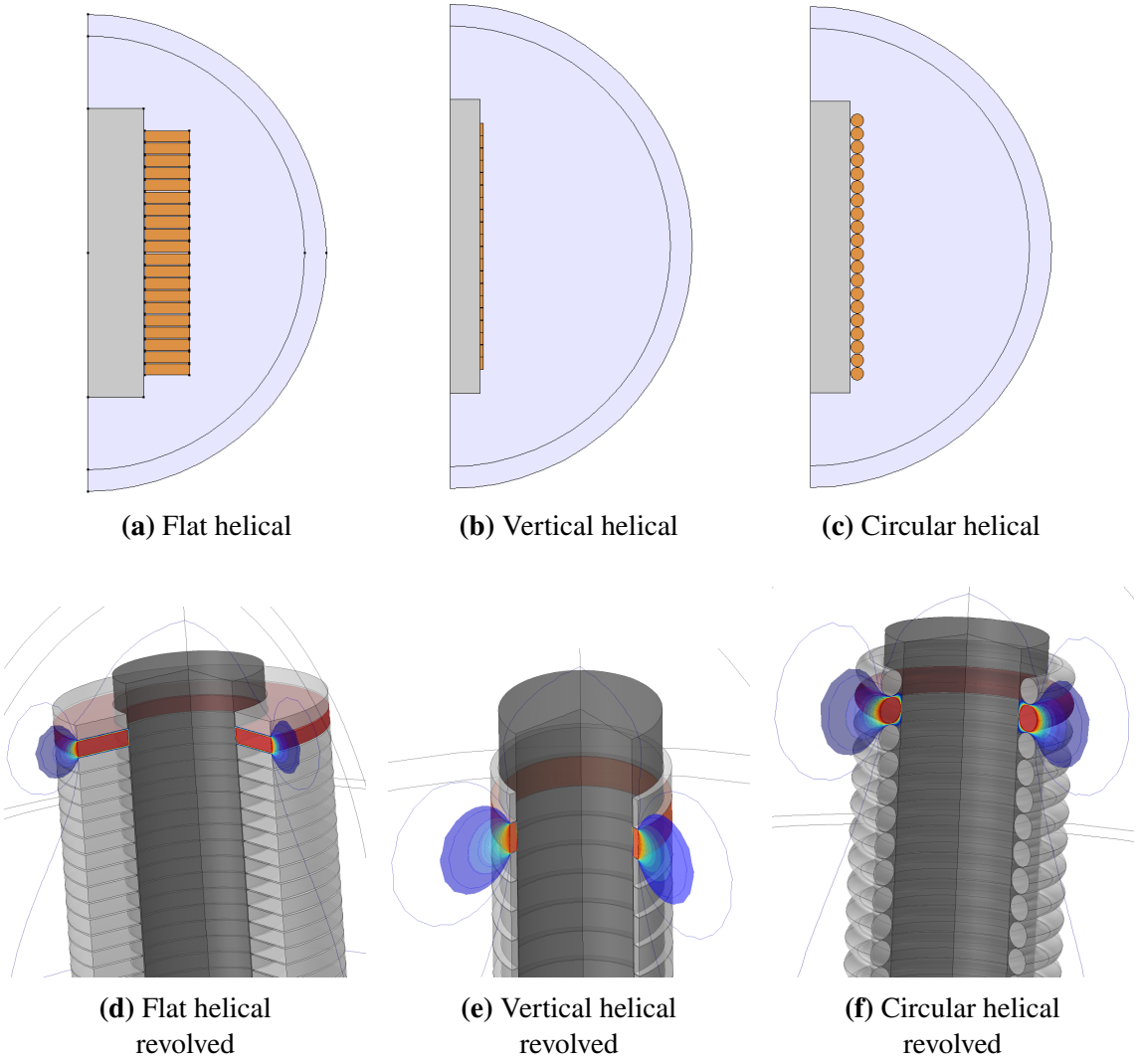

(a) Flat helical

(b) Vertical helical

(c) Circular helical

(d) Flat helical revolved

(e) Vertical helical revolved

(f) Circular helical revolved

Figure 11.1: The three proposed inductor designs as created in a 2D axis symmetric environment. The bottom row shows the respective designs when revolved 270°with voltage applied to the second terminal. The contour plot is the electric field lines.

1. Large surface areas gives high capacitance.

2. Small increase in distance between turns gives large decrease in capacitance.

3. Change in distance between winding and core has little impact on capacitance.

Figure 11.2 show how the lumped parallel capacitance for each of the three inductors change when increasing the turn-to-turn distance. It clearly show how the flat helical inductor suffers from its large turn-to-turn surface area. It is also seen that increasing the distance by just 0.2 mm more than halves the capacitance for this type of winding.

The circular profile had the smallest amount of parasitic capacitance. This was as expected due to the nature of circles which increases the inter-turn distance when moving away from the center of the conductor.

When keeping the turn-to-turn distance constant while increasing the distance between the core and the winding, the results is less significant. Figure 11.4 show almost no change in parasitic capacitance. Instead it shows a small increase.

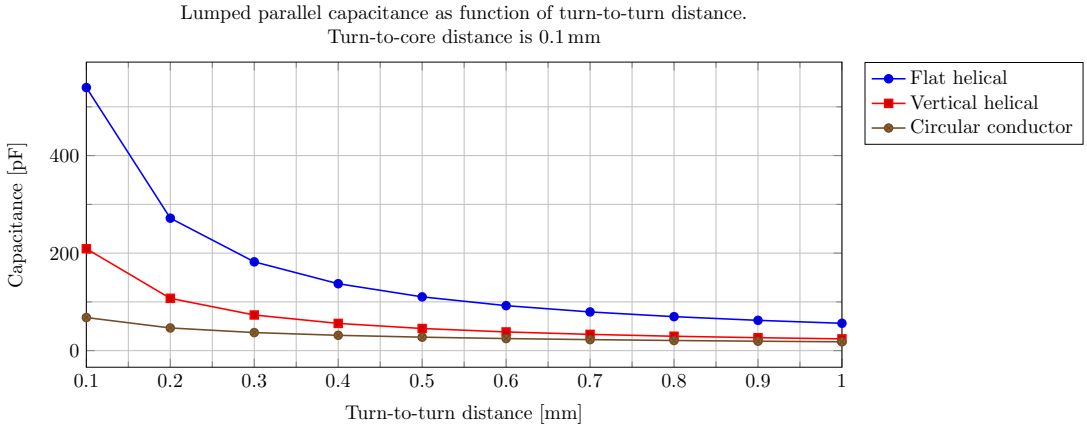

Figure 11.2: Graph showing lumped parallel capacitance for the three different winding profiles as function of distance between turns. The turn-to-core distance is fixed, and the core is conducting and grounded.

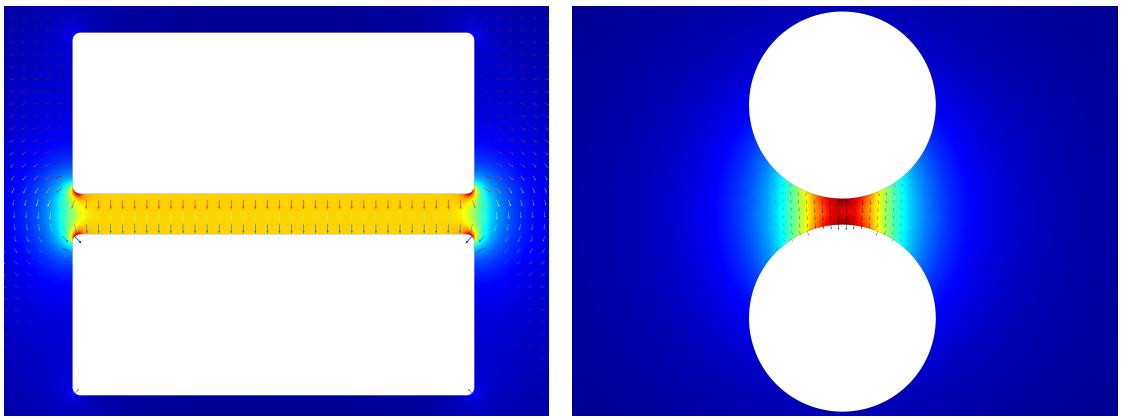

(a) Flat helical conductors **(b)** Circular conductors

Figure 11.3: Electrostatic field simulation comparing the electric field strength between two rectangular conductors and two circular conductors. The distance between the two conductors are equal in both figures.

Table 11.1: Total stray capacitances

Turn-to turn Distance [mm]	Model-1: Flat Helical Core $r = 25$ mm [pF]	Model-2: Vertical Helical Core $r = 35$ mm [pF]	Model-3: Circular Helical Core $r = 50$ mm [pF]
0.1	542.56	216.73	70.66
0.2	274.61	114.84	49.29
0.3	185.01	80.54	39.84
0.4	140.08	63.15	34.20
0.5	113.08	52.57	30.37
0.6	94.98	45.41	27.54
0.7	82.05	40.29	25.34
0.8	72.34	36.33	23.57
0.9	64.73	33.31	22.11
1	58.63	30.79	20.87

11.1.1 Comparison

Because the three inductor designs have different core radius, the different results reflect not only the effect of varying winding profile, but also the variance in winding length and the total area between adjacent turns.

Due to this, the results in table 11.1 are not directly comparable to each other when comparing winding profile.

To make comparable results with respect to winding profile alone, new simulations were conducted with identical core radius: 20 mm. These results are shown in table 11.2.

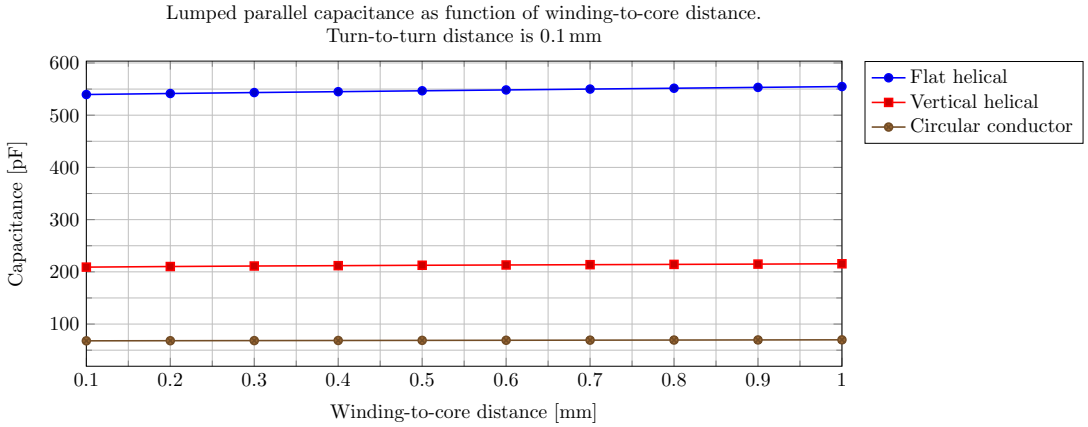

Figure 11.4: Graph showing lumped parallel capacitance for the three different winding profiles as function of distance between core and winding. The turn-to-turn distance is fixed, and the core is conducting and grounded.

Table 11.2: Total stray capacitances (same core radius for comparison)

Turn-to-turn Distance [mm]	Model-1: Flat Helical [pF]	Model-2: Vertical Helical [pF]	Model-3: Circular Helical [pF]
0.1	465.27	92.94	43.05
0.2	235.48	49.24	29.55
0.3	158.66	34.47	23.57
0.4	120.13	27.01	20.02
0.5	96.96	22.46	17.59
0.6	81.45	19.37	15.81
0.7	70.35	17.18	14.42
0.8	62.02	15.50	13.31
0.9	55.50	14.18	12.38
1	50.27	13.08	11.60

12. SIMULINK testing of inductor

This chapter presents the simulation results when employing the modeled inductors with stray capacitance.

As the inductance values differ, the filter capacitor is adjusted accordingly to maintain the same cutoff frequency for all three filters.

12.1 Model-1: Flat helical inductor

Filter parameters: L_f =211.9 µH, C_f = 159.72 µF.

With the lowest gap distance, 0.1 mm, this inductor exhibit a stray parallel capacitance of 542.56 pF.

When applying PWM-voltage with infinite rise time to this filter, there are clear signs of both voltage doubling at the motor terminals and reflections. This is illustrated in figure 12.1a and 12.1b. It is seen that the reflections alternate between the filter output (blue trend) and the motor terminals (red trend). These reflections are slowly decaying until completely faded after approximately 75 µs.

The maximum voltage recorded was 1622 V which is quite close to a doubling of the DC-link voltage (813 V).

The time between reflections are 1.233 µs. This agrees closely to (5.7); the expected reflection time for a 50 m cable with parameters as shown in table 12.1:

$$\tau_{reflection} = 2 \cdot 0.5\,\text{km} \cdot \sqrt{0.2414\,\text{mH} \cdot 0.615\,\mu\text{F}} = 1.218\,\mu\text{s} \tag{12.1}$$

Increasing the gap distance to 0.2 mm reduces the stray capacitance to 274.61 pF (table 11.1), but this does not suffice to mitigate reflections (figure 12.1c).

Further increase of turn-to-turn distance, this time to 0.3 mm, finally reduces the stray capacitance sufficiently to prevent reflections. The stray capacitance is now 185.01 pF.

The output voltage waveform is seen as very smooth in figure 12.1d with a maximum recorded voltage peak of 989.3 V (1.22 per-unit).

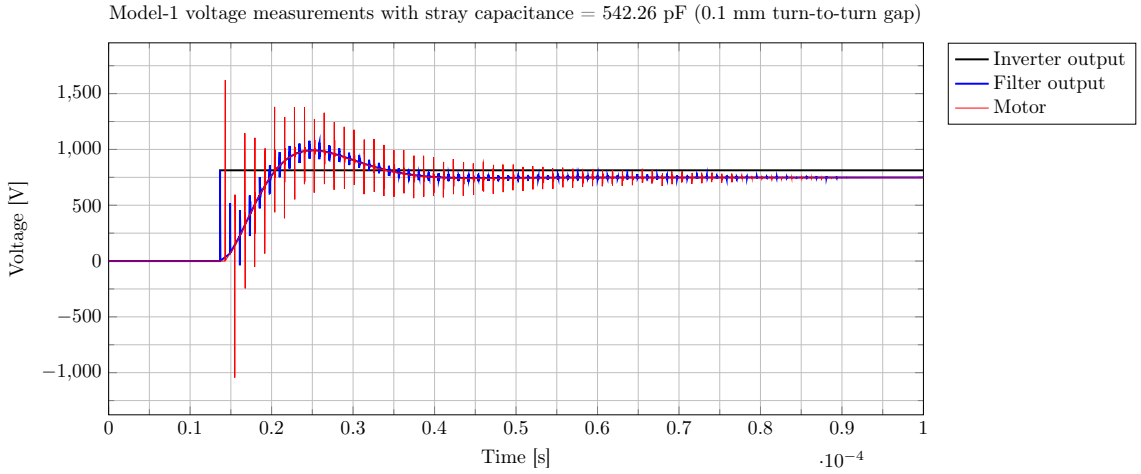

(a) Reflections occur when the series capacitance is too large.

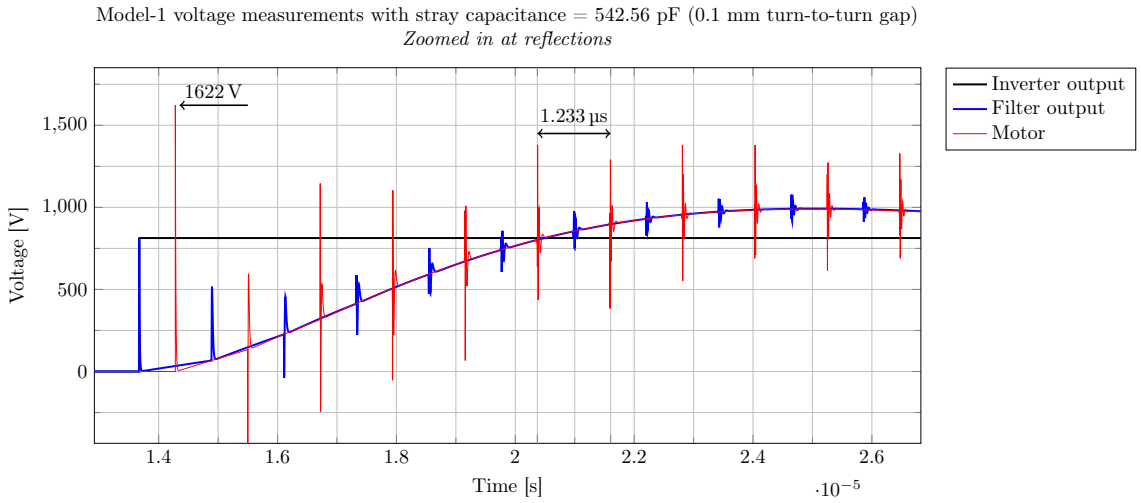

(b) A zoomed in view at the voltage doubling and the reflections.

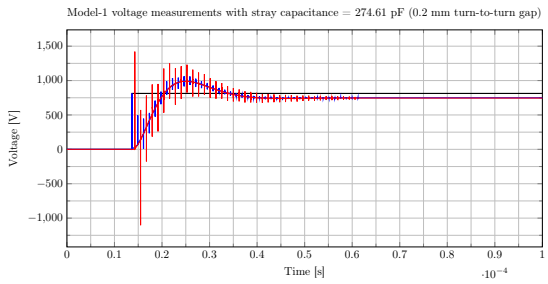

(c) Reflections still occur at turn-to-turn distance = 0.2 mm

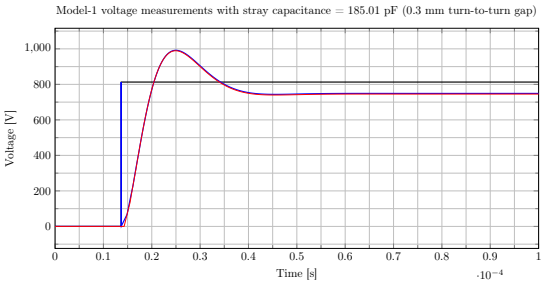

(d) Reflections mitigated at 0.3 mm

Figure 12.1: Simulation results of dV/dt filter with inductor parameters from Model-1

12.2 Model-2: Vertical helical inductor

Filter parameters: L_f =216.8 µH, C_f = 156.11 µF.

Table 12.1: Cable data for motor cable

Property	Symbol	Value	Unit	Comment
Cable inductance	L_c	0.2414	mH/km	
Cable capacitance	C_c	0.615	µF/km	estimated by Draka

Table 12.2: Summary of results from SIMULINK testing of filter inductors with stray parallel capacitance

Filter inductor	L_f	C_f	K_{sp}	$\hat{V}_{Vmax}$	Reflection
Model-1: 0.1 mm	211.9 µH	159.7 µF	542.56 pF	1622 V	Yes
Model-1: 0.2 mm	211.9 µH	159.7 µF	274.61 pF	1622 V	Yes
Model-1: 0.3 mm	211.9 µH	159.7 µF	185.01 pF	989.3 V	No
Model-2: 0.1 mm	216.8 µH	156.1 µF	216.73 pF	1622 V	Yes
Model-2: 0.2 mm	216.8 µH	156.1 µF	114.84 pF	991.1 V	No
Model-3: 0.1 mm	215.5 µH	157.1 µF	70.66 pF	990.4 V	No

The inductor with vertical helical winding had considerably lower inductance as the contact area between turns are five times smaller than the flat vertical winding.

The distance between gap and core and between winding turns is 0.1 mm. This yields a stray series capacitance of 216.73 pF. Figure 12.2a shows that reflections are occurring also at this capacitance value.

Increasing the turn-to-turn distance to 0.2 mm reduces the capacitance value to 114.84 pF, which is lower than the reflection-seizing value from Model-1. Figure 12.2b shows a clean voltage waveform with a peak voltage of 991.1 V (1.22 per-unit).

12.3 Model-3: Circular helical inductor

Filter parameters: L=215.5 uH, C = 157.05 uF

The circular shaped profile demonstrates a very low stray capacitance between turns, and thus reflections does not occur even at the lowest distance. Figure 12.3a shows a smooth voltage waveform with a peak voltage at 990.4 V (1.22 per-unit).

12.4 Summary

A summary of the three filter inductors are presented in table 12.2. It is seen that both flat and vertical conductors needed a slight increase of turn-to-turn distance to avoid reflections and voltage doubling at the motor terminals.

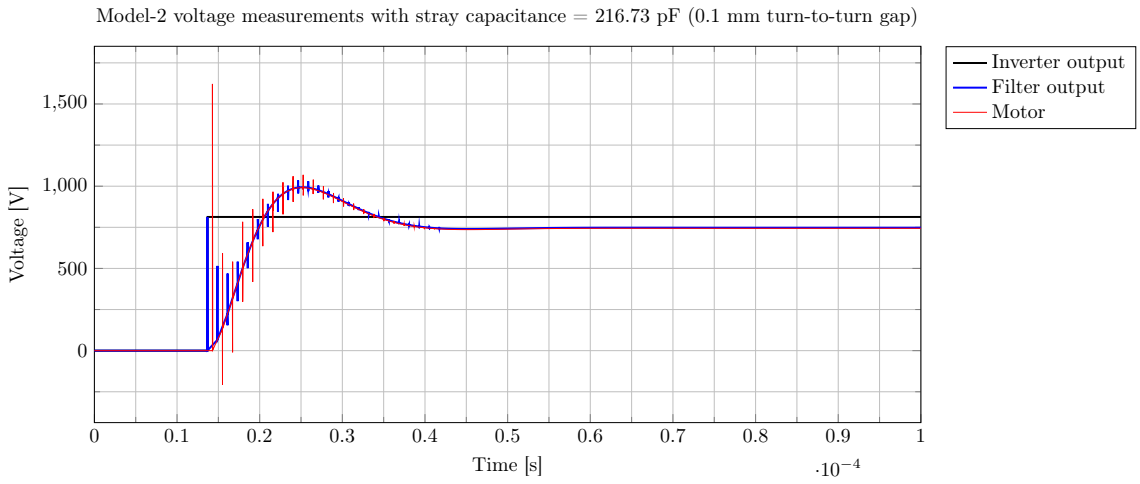

(a) Reflections at 0.1 mm

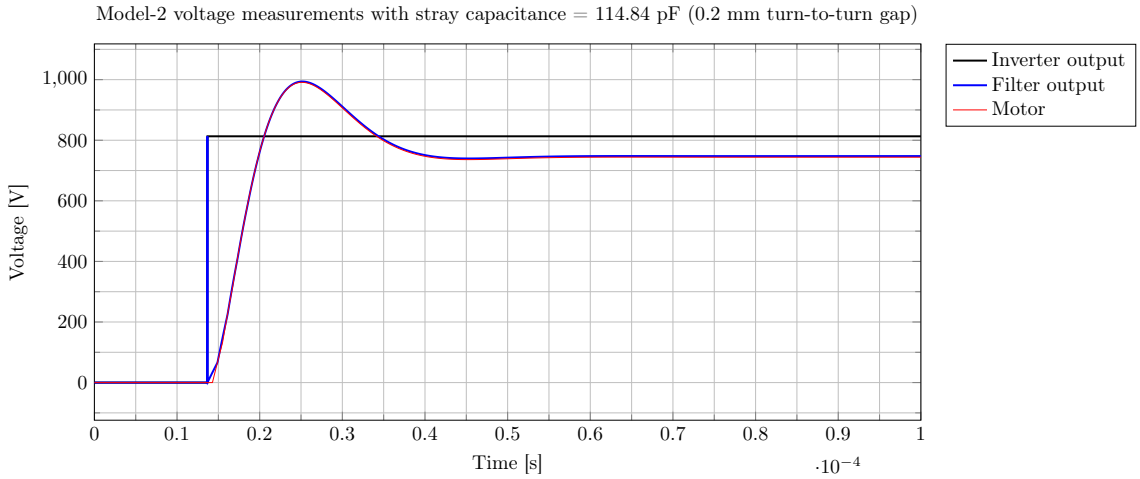

(b) No reflections at 0.2 mm

Figure 12.2: Simulation results of dV/dt filter with inductor parameters from Model-2

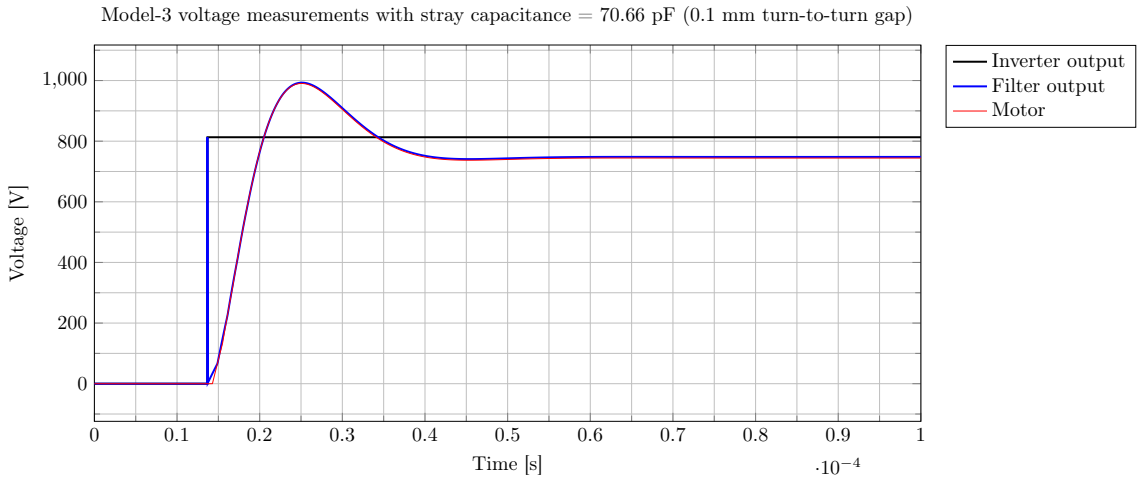

(a) Reflections occur when the series capacitance is too large.

Figure 12.3: Simulation results of dV/dt filter with inductor parameters from Model-3

Part IV

Conclusion and further work

13. Conclusion

The work in this report has examined design of high-powered filter inductors for use in power electronics with fast rise time with respect to low stray capacitance.

Three different filter inductors were designed in COMSOL to ascertain the impact conductor profile has on stray capacitance. The three profiles were flat helical, vertical helical and circular.

The inductors were designed with commercially available core material with efforts to keep it compact while sustaining the amount of flux needed without saturating. The chosen material was Fe-Ni based powder due to its low losses and high saturation flux density.

The inductors were tested with different geometric distances between turns and between core and winding to study the impact on stray capacitance. It was found that the most compact design was flat helical winding, but it also had the highest amount of stray capacitance. This could be halved by increasing the turn to turn distance by just 0.1 mm.

All three inductors exhibited reduction in stray capacitance when increasing turn to turn distance, but the sharpest decrease was found with the flat helical profile.

The inductors were tested in SIMULINK with various values of stray capacitance to check how series capacitance affects filter performance. At values above approximately 200 pF, the filter sustained reflections and voltage doubling at the motor terminals. Reducing stray capacitance by increasing turn to turn distance mitigated this problem, and filter performance was found satisfactory.

The inverter output rise time simulated in this report is infinite, which is impossible for practical devices. Also the stray parallel capacitance is modeled as one single capacitor while it in reality composes of a network of series and parallel capacitor which all needs to be charged in a given sequence. These two aspects contributes to making the results a worst case scenario. This is intentional because it provides a positive margin of error. It can also make prototypes based on this approach over-compensated for the effect - which is why practical experiments are important to avoid excessive measures to be taken when they are not needed.

14. Further work

This work has utilized COMSOL for the majority of simulations. Still, many other possibilities exist that time did not allow for the duration of this thesis.

These possibilities are suggested for further work to enhance inductor design and testing:

- Utilize thermal studies to optimize inductor design with regards to cooling and current carrying capabilities.
- Employ the built-in circuit feature to apply PWM voltage to the inductor terminals.
- Conduct *LiveLink*-studies which couples COMSOL-models to SIMULINK.
- Perform parametric sweeps with regards to optimal design using the COMSOL optimizer feature.

A last suggestion is of course the practical design of the proposed inductors so that real tests and measurements performed.

Bibliography

[1] Y Solbakken. *Use of SiC Devices in Maritime Applications*. English. Project Report. Trondheim: Norwegian University of Science and Technology, Dec. 2015.

[2] Junping He, Wei Chen, and Jianguo Jiang. "Identification and improvement of stray coupling effect in an L-C-L common mode EMI filter". In: *Power Electronics and Motion Control Conference, 2006. IPEMC 2006. CES/IEEE 5th International*. Vol. 2. Aug. 2006, pp. 1–5. DOI: 10.1109/IPEMC.2006.4778157.

[3] T. C. Neugebauer and D. J. Perreault. "Parasitic capacitance cancellation in filter inductors". In: *Power Electronics Specialists Conference, 2004. PESC 04. 2004 IEEE 35th Annual*. Vol. 4. 2004, 3102–3107 Vol.4. DOI: 10.1109/PESC.2004.1355331.

[4] M. B. Shadmand and R. S. Balog. "FEA tool approach for determination of parasitic capacitance of the windings in high frequency coupled inductors filters". In: *2012 IEEE Power and Energy Conference at Illinois (PECI)*. Feb. 2012, pp. 1–5. DOI: 10.1109/PECI.2012.6184580.

[5] A Nysveen. *Power Transformers*. 2015th ed. TET4195 High Voltage Equipment. Trondheim, 2015.

[6] A. Massarini, M.K. Kazimierczuk, and G. Grandi. "Lumped parameter models for single- and multiple-layer inductors". In: *, 27th Annual IEEE Power Electronics Specialists Conference, 1996. PESC '96 Record*. Vol. 1. June 1996, 295–301 vol.1. DOI: 10.1109/PESC.1996.548595.

[7] A. Massarini and M.K. Kazimierczuk. "Self-capacitance of inductors". In: *IEEE Transactions on Power Electronics* 12.4 (July 1997), pp. 671–676. ISSN: 0885-8993. DOI: 10.1109/63.602562.

[8] Ned Mohan, Tore M. Undeland, and William P. Robbins. *Power Electronics: Converters, Applications, and Design*. English. 3 edition. Hoboken, NJ: Wiley, Oct. 2002. ISBN: 978-0-471-22693-2.

[9] J Skaar. *Kompendium i TET4120 Elektromagnetisme*. NTNU / Akademika Forlag, Nov. 2013.

[10] A. Stadler, T. Stolzke, and C. Gulden. "Design and Simulation of Thermally Optimized Filter Inductors for a 1MW Windmill Demonstrator". In: *Renewable Energy and Energy Management; Proceedings of PCIM Europe 2015; International Exhibition and Conference for Power Electronics, Intelligent Motion*. May 2015, pp. 1–5.

[11] Mark A. Swihart. *Inductor Cores Material and Shape Choices*. 2013.

[12] A. Stadler. "InDUR Power Inductors with Minimum Size and Weight for DC and AC Filter Applications". In: *Bodos Power Systems Magazine* Jan 2014 (Jan. 2014), pp. 36–38. URL: http://www.bodospower.com/restricted/downloads/bp_2014_01.pdf.

[13] A. Stadler, T. Stolzke, and C. Gulden. "A new generation of modular power inductors with minimum thermal resistance". In: *2014 16th European Conference on Power Electronics and Applications (EPE'14-ECCE Europe)*. Aug. 2014, pp. 1–7. DOI: 10.1109/EPE.2014.6910771.

[14] A. Stadler, T. Stolzke, and C. Gulden. "High frequency high current filter inductors with minimum thermal resistance". In: *Power Electronics and Motion Control Conference and Exposition (PEMC), 2014 16th International*. Sept. 2014, pp. 289–292. DOI: 10.1109/EPEPEMC.2014.6980507.

[15] B. G. You et al. "Comparison of simulation and experimental results for Mega Flux inductors in Hybrid Electric Vehicles". In: *2011 IEEE 8th International Conference on Power Electronics and ECCE Asia (ICPE ECCE)*. May 2011, pp. 1950–1957. DOI: 10.1109/ICPE.2011.5944442.

[16] S. Schmitt. "Acoustic noise of sheeted electrical steel inductors in PWM operation #x2014; causes and mitigation". In: *13th European Conference on Power Electronics and Applications, 2009. EPE '09*. Sept. 2009, pp. 1–8.

[17] T. Hatakeyama and K. Onda. "Core Loss Estimation of Various Materials Magnetized With the Symmetrical/Asymmetrical Rectangular Voltage". In: *IEEE Transactions on Power Electronics* 29.12 (Dec. 2014), pp. 6628–6635. ISSN: 0885-8993. DOI: 10.1109/TPEL.2014.2306755.

[18] Martin Ferch. *Nanocrystalline core materials for modern power electronic designs*. Apr. 2003. URL: http://www.magnetec.de/fileadmin/pdf/np_powerelectronic_e.pdf.

[19] J. Kindmark and F. Rosén. “Powder Material for Inductor Cores - Evaluation of MPP, Sendust and High flux core characteristics”. Master Thesis. Göteborg, Sweden: Chalmers University of Technology, 2013.

[20] Y. Yoshizawa and K. Yamauchi. “Induced Magnetic Anisotropy and Thickness Dependence of Magnetic Properties in Nanocrystalline Alloy "Finemet"”. In: *IEEE Translation Journal on Magnetics in Japan* 5.11 (Nov. 1990), pp. 1070–1076. ISSN: 0882-4959. DOI: 10.1109/TJMJ.1990.4564397.

[21] M. S. Rylko et al. “Magnetic material comparisons for high-current gapped and gapless foil wound inductors in high frequency dc-dc converters”. In: *Power Electronics and Motion Control Conference, 2008. EPE-PEMC 2008. 13th*. Sept. 2008, pp. 1249–1256. DOI: 10.1109/EPEPEMC.2008.4635440.

[22] Yu-Ming Kuo and Jenq-Gong Duh. “Application of nanocrystalline FeHfN soft magnetic films to power inductors”. In: *Journal of Magnetism and Magnetic Materials* 324.6 (Mar. 2012), pp. 1084–1087. ISSN: 0304-8853. DOI: 10.1016/j.jmmm.2011.10.029. URL: http://www.sciencedirect.com/science/article/pii/S0304885311007372 (visited on 06/02/2016).

[23] A. Roch and F. Leferink. “Nanocrystalline Core Material for High-Performance Common Mode Inductors”. In: *IEEE Transactions on Electromagnetic Compatibility* 54.4 (Aug. 2012), pp. 785–791. ISSN: 0018-9375. DOI: 10.1109/TEMC.2012.2188103.

[24] D. P. Urciuoli and T. E. Salem. “New Nanocrystalline Core Performance Versus Finemet(Registered) for High-power Inductors”. In: *ResearchGate* (Nov. 2008), p. 5. URL: https://www.researchgate.net/publication/235087613_New_Nanocrystalline_Core_Performance_Versus_FinemetRegistered_for_High-power_Inductors (visited on 06/02/2016).

[25] Jianguo Long et al. “Nanocrystalline material development for high-power inductors”. In: *Journal of Applied Physics* 103.7 (Apr. 2008), 07E705. ISSN: 0021-8979, 1089-7550. DOI: 10.1063/1.2829033. URL: http://scitation.aip.org/content/aip/journal/jap/103/7/10.1063/1.2829033 (visited on 06/02/2016).

[26] T. E. Salem et al. “Design Considerations for High Power Inductors in DC-DC Converters”. In: *APEC 07 - Twenty-Second Annual IEEE Applied Power Electronics Conference and Exposition*. Feb. 2007, pp. 1258–1263. DOI: 10.1109/APEX.2007.357676.

[27] H. J. Liu et al. “Effect of Particle Size Distribution on the Magnetic Properties of Fe-Si-Al Powder Core”. en. In: *Journal of Superconductivity and Novel Magnetism* 29.2 (Nov. 2015), pp. 463–468. ISSN: 1557-1939, 1557-1947. DOI: 10.1007/s10948-015-3282-4. URL: http://link.springer.com/article/10.1007/s10948-015-3282-4 (visited on 06/02/2016).

[28] P. Gramatyka et al. “Nanocrystalline iron based powder cores for high frequency applications”. In: *Journal of Achievements in Materials and Manufacturing Engineering* 18.1-2 (Sept. 2006), pp. 99–102.

[29] M. S. Rylko et al. “Revised Magnetics Performance Factors and Experimental Comparison of High-Flux Materials for High-Current DC #x2013;DC Inductors”. In: *IEEE Transactions on Power Electronics* 26.8 (Aug. 2011), pp. 2112–2126. ISSN: 0885-8993. DOI: 10.1109/TPEL.2010.2103573.

[30] J. R. R. Zientarski et al. “A design methodology for optimizing the volume in single-layer inductors applied to PFC boost converters”. In: *2009 Brazilian Power Electronics Conference*. Sept. 2009, pp. 1177–1184. DOI: 10.1109/COBEP.2009.5347617.

[31] K. Yanagimoto et al. “Effect of Si and Al content on core loss in Fe-Si-Al powder cores”. In: *IEEE Transactions on Magnetics* 40.3 (May 2004), pp. 1691–1694. ISSN: 0018-9464. DOI: 10.1109/TMAG.2004.826623.

[32] H. C. Sartori, J. E. Baggio, and J. R. Pinheiro. “A comparative design of an optmized boost inductor taking into account three magnetic materials technologies: Volume, cost and efficiency analysis”. In: *2012 10th IEEE/IAS International Conference on Industry Applications (INDUSCON)*. Nov. 2012, pp. 1–6. DOI: 10.1109/INDUSCON.2012.6452415.

[33] A. Alabakhshizadeh, O. M. Midtgård, and K. Boysen. “Analysis, design, and evaluation of a high frequency inductor to reduce manufacturing cost, and improve the efficiency of a PV inverter”. In: *2013 IEEE 39th Photovoltaic Specialists Conference (PVSC)*. June 2013, pp. 2845–2848. DOI: 10.1109/PVSC.2013.6745064.

[34] Y. Miwa and T. Shimizu. “Loss comparison of inductors used for buck-chopper circuit”. In: *2015 9th International Conference on Power Electronics and ECCE Asia (ICPE-ECCE Asia)*. June 2015, pp. 2098–2103. DOI: 10.1109/ICPE.2015.7168067.

[35] Magnetics Inc. *Product Catalog 2015 - Magnetic Powder Cores*. URL: https://www.mag-inc.com/File%20Library/Product%20Literature/Powder%20Core%20Literature/2015-Magnetics-Powder-Core-Catalog.pdf (visited on 06/06/2016).

[36] Chang Sung Corporation. *Magnetic Powder Core Catalog*. 13th ed. Chang Sung Corporation.

[37] NCD. *Product Catalog 2015 - Magnetic Powder Cores*.

[38] D. C. Pentz. "Overview of helical foil winding design for planar magnetic components". In: *2013 IEEE International Conference on Industrial Technology (ICIT)*. Feb. 2013, pp. 628–632. DOI: 10.1109/ICIT.2013.6505744.

[39] M. Zdanowski et al. "Design and evaluation of reduced self-capacitance inductor for fast-switching SiC BJT dc/dc converters". In: *Power Electronics and Motion Control Conference (EPE/PEMC), 2012 15th International*. Sept. 2012, DS1a.4–1–DS1a.4–7. DOI: 10.1109/EPEPEMC.2012.6397194.

List of Figures

List of Tables

Appendices

A. Simulink model to test filter designs

Filter_IM_with_stray_parallel_only

Details for Filter_IM_with_stray_parallel_only and below

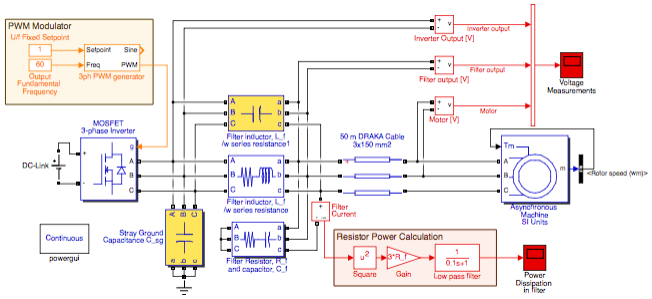

Yngve

03-Jul-2016 16:22:08

Table of Contents

List of Tables

Model - Filter_IM_with_stray_parallel_only

Full Model Hierarchy

1. Filter_IM_with_stray_parallel_only
    1. 3ph PWM generator

Simulation Parameter	Value
Solver	ode23t
RelTol	1e-7
Refine	1
MaxOrder	5

ZeroCross	on

[more info]

System - Filter_IM_with_stray_parallel_only

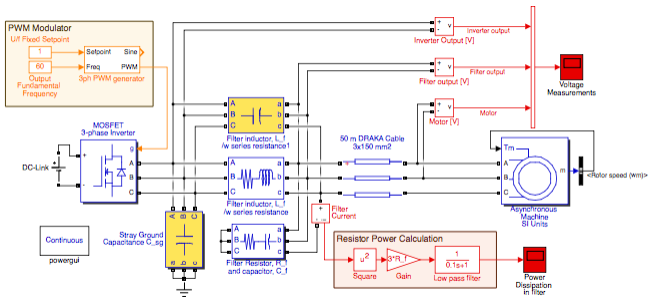

Table 1. Asynchronous Machine Block Properties

Name	Rotor Type	Preset Model	Mechanical Load	Reference Frame	Measurement Bus	Nominal Parameters	Stator	Rotor	Lm	Mechanical	Initial Conditions	Simulate Saturation	Saturation	Ts Bl
Asynchronous Machine SI Units	Squirrel-cage	11: 50 HP 575 V 60Hz 1775 RPM	Torque Tm	Synchronous	off	[3.73e+04 575 60]	[0.09871 0.001245]	[0.1081 0.001245]	0.04717	[0.4 0.02481 2]	[1 0 0 0 0 0 0 0]	off	[14.03593122, 27.81365428, 53.79336849, 72.68890987, 97.98006896, 148.6815601, 215.7428561, 302.9841135, 420.4778367 ; 230, 322, 414, 460, 506, 552, 598, 644, 690]	-1

Table 2. BusSelector Block Properties

Name	Output Signals	Output As Bus	Input Signals
Bus Selector	Mechanical.Rotor speed (wm)	off	{ Rotor measurements , Rotor current ir_a (A) Rotor current ir_b (A) Rotor current ir_c (A) Rotor current iq (A) Rotor current id (A) Rotor flux phir_q (V s) Rotor flux phir_d (V s) Rotor voltage Vr_q (V) Rotor voltage Vr_d (V) } { Stator measurements , Stator current is_a (A) Stator current is_b (A) Stator current is_c (A) Stator current is_q (A) Stator current is_d (A) Stator flux phis_q (V s) Stator flux phis_d (V s) Stator voltage vs_q (V) Stator voltage vs_d (V) } Lm (H) { Mechanical , Rotor speed (wm) Electromagnetic torque Te (N*m) Rotor angle thetam (rad) }

Table 3. Constant Block Properties

Name	Value	Out Data Type Str	Lock Scale	Sample Time	Frame Period
Output Fundamental Frequency	60	Inherit: Inherit from 'Constant value'	off	inf	inf
U/f Fixed Setpoint	1	Inherit: Inherit from 'Constant value'	off	inf	inf

Table 4. Current Measurement Block Properties

Name	Output Type
Filter Current	Complex

Table 5. DC Voltage Source Block Properties

Name	Amplitude	Measurements

DC-Link	813	None

Table 6. Distributed Parameters Line Block Properties

Name	Phases	Frequency	Resistance	Inductance	Capacitance	Length	Measurements
50 m DRAKA Cable 3x150 mm2	3	60	[R_c R_0]	[L_c L_0]	[C_c C_0]	1	None

Table 7. Gain Block Properties

Name	Gain	Multiplication	Param Data Type Str	Out Data Type Str	Lock Scale	Rnd Meth	Saturate On Integer Overflow
Gain	3*R_f	Element-wise(K.*u)	Inherit: Inherit via internal rule	Inherit: Inherit via internal rule	off	Floor	off

Table 8. Ground Block Properties

Name	Physical Domain	Sub Class Name	Left Port Type	Right Port Type
Ground	powersysdomain	unknown	p1	p1

Table 9. Math Block Properties

Name	Operator	Output Signal Type	Out Data Type Str	Lock Scale	Rnd Meth	Saturate On Integer Overflow	Intermediate Results Data Type Str	Algorithm Type	Iterations
Square	square	auto	Inherit: Same as first input	off	Floor	on	Inherit: Inherit via internal rule	Newton-Raphson	3

Table 10. Mux Block Properties

Name	Inputs	Display Option
Mux	3	bar

Table 11. PSB option menu block Block Properties

Name	Simulation Mode	SPID	Interpol	Methode	Function Messages	Echomessages	Enable Use Of TLC	X0status	Frequencyindice	Pbase	Err Max	Iterations	Units V	Units W
powergui	Continuous	off	off	off	off	off	off	blocks	0	100e6	1e-4	50	kV	MW

Table 12. Three-Phase Parallel RLC Branch Block Properties

Name	Branch Type	Resistance	Inductance	Capacitance	Measurements
Stray Ground Capacitance C_sg	C	1	L_f	1e-12	None

Table 13. Three-Phase Series RLC Branch Block Properties

Name	Branch Type	Resistance	Inductance	Capacitance	Measurements
Filter inductor, L_f /w series resistance	RL	3e-3	L_f	1e-6	Branch voltages and currents
Filter inductor, L_f /w series resistance1	C	3e-3	L_f	70.66e-12	Branch voltages and currents
Filter Resistor, R_f and capacitor, C_f	RC	R_f	1e-3	C_f	None

Table 14. TransferFcn Block Properties

Name	Numerator	Denominator	Absolute Tolerance	Continuous State Attributes
Low pass filter	[1]	[0.1 1]	auto	''

Table 15. Universal Bridge Block Properties

Name	Arms	Snubber Resistance	Snubber Capacitance	Device	Ron	Measurements
MOSFET 3-phase Inverter	3	1e5	inf	MOSFET / Diodes	1e-3	None

Table 16. Voltage Measurement Block Properties

Name	Output Type
Filter output [V]	Complex
Inverter Output [V]	Complex
Motor [V]	Complex

System - Filter_IM_with_stray_parallel_only/3ph PWM generator

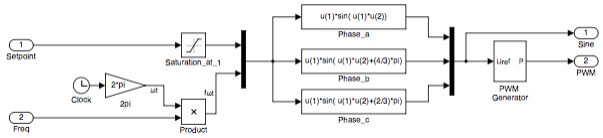

Table 17. Clock Block Properties

Name	Display Time	Decimation
Clock	off	1

Table 18. Fcn Block Properties

Name	Expr
Phase_a	u(1)*sin(u(1)*u(2))
Phase_b	u(1)*sin(u(1)*u(2)+(4/3)*pi)
Phase_c	u(1)*sin(u(1)*u(2)+(2/3)*pi)

Table 19. Gain Block Properties

Name	Gain	Multiplication	Param Data Type Str	Out Data Type Str	Lock Scale	Rnd Meth	Saturate On Integer Overflow
2pi	2*pi	Element-wise(K.*u)	Inherit: Inherit via internal rule	Inherit: Inherit via internal rule	off	Floor	off

Table 20. Inport Block Properties

Name	Port	Defined In Blk
Freq	2	Output Fundamental Frequency
Setpoint	1	U/f Fixed Setpoint

Table 21. Mux Block Properties

Name	Inputs	Display Option
Mux	3	bar
Mux1	2	bar

Table 22. Outport Block Properties

Name	Port	Icon Display	Lock Scale	Var Size Sig	Signal Type	Sampling Mode	Source Of Initial Output Value	Output When Disabled	Used By Blk
PWM	2	Port number	off	Inherit	auto	auto	Dialog	held	Data Type Conversion
Sine	1	Port number	off	Inherit	auto	auto	Dialog	held	Zero-Order Hold, m, Selector_FullBridgeIn, Selector_FullBridgeIn, Relational Operator2, Zero-Order Hold, end

Table 23. PWM Generator (2-Level) Block Properties

Name	Modulator Type	Modulator Mode	Fc	Pc	Min Max	Sampling Technique	Modulating Signals	Ts	Show Carrier Outport
PWM Generator	Three-phase bridge (6 pulses)	Unsynchronized	f_s	90	[-1 1]	Natural	off	0	off

Table 24. Product Block Properties

Name	Inputs	Multiplication	Collapse Mode	Collapse Dim	Input Same DT	Out Data Type Str	Lock Scale	Rnd Meth	Saturate On Integer Overflow
Product	2	Element-wise(.*)	All dimensions	1	off	Inherit: Inherit via internal rule	off	Floor	off

Table 25. Saturate Block Properties

Name	Upper Limit	Lower Limit	Linearize As Gain	Zero Cross	Out Data Type Str	Lock Scale	Rnd Meth
Saturation_at_1	1	0	on	on	Inherit: Same as input	off	Floor

Appendix

Table 26. Block Type Count

BlockType	Count	Block Names
Voltage Measurement (m)	3	Filter output [V], Inverter Output [V], Motor [V]
Three-Phase Series RLC Branch (m)	3	Filter Resistor, R_f and capacitor, C_f, Filter inductor, L_f /w series resistance, Filter inductor, L_f /w series resistance1
Mux	3	Mux, Mux1, Mux
Fcn	3	Phase_a, Phase_b, Phase_c
Scope	2	Power Dissipation in filter, Voltage Measurements
Outport	2	PWM, Sine
Inport	2	Freq, Setpoint
Gain	2	2pi, Gain
Constant	2	Output Fundamental Frequency, U/f Fixed Setpoint
Universal Bridge (m)	1	MOSFET 3-phase Inverter
TransferFcn	1	Low pass filter
Three-Phase Parallel RLC Branch (m)	1	Stray Ground Capacitance C_sg
SubSystem	1	3ph PWM generator
Saturate	1	Saturation_at_1
Product	1	Product
PWM Generator (2-Level) (m)	1	PWM Generator
PSB option menu block (m)	1	powergui
Math	1	Square
Ground (m)	1	Ground
Distributed Parameters Line (m)	1	50 m DRAKA Cable 3x150 mm2
DC Voltage Source (m)	1	DC-Link
Current Measurement (m)	1	Filter Current
Clock	1	Clock
BusSelector	1	Bus Selector
Asynchronous Machine (m)	1	Asynchronous Machine SI Units

Table 27. Model Functions

Function Name	Parent Blocks	Calling string
pi	2pi	`2*pi`